Impact of humid supercritical CO_2 flow and CO_2 solvation-induced cement porewater expulsion on reactive self-sealing processes along wellbore microannuli

T.K.T. Wolterbeek [a,b,*], J.R. Snippe [b], S.J.T. Hangx [a]

[a] *Department of Earth Sciences, Utrecht University, Princetonlaan 4, 3584 CB, Utrecht, the Netherlands*
[b] *Shell Global Solutions International B.V., Grasweg 31, 1031 HW, Amsterdam, the Netherlands*

ABSTRACT

Ensuring geological containment of injected CO_2 is a key requirement in the planning and execution of Carbon Capture and Storage (CCS) projects. This includes a proper analysis, and if needed remediation, of the wellbore cement sealing integrity. Defects like casing-cement microannuli can impair this sealing integrity, especially if they expose the cement to flowing CO_2-rich fluids. Chemical reaction between the cement and CO_2 could in specific cases potentially enlarge seepage pathways, while in others reaction may seal off pathways via carbonate precipitation. Previous studies focused on these reactive transport processes during flow of CO_2-rich brine, demonstrating small cement defects possess some definite capacity to self-seal. While this earlier work produced valuable insight, water-based flow experiments are not fully representative for CO_2 seepage along real CCS wells. Actual seepage flows will likely be buoyancy-driven and consist mainly of humid CO_2 (in its gaseous, liquid, or supercritical phase) rather than carbonated brine. Humid CO_2 and carbonated brine have very different fluid properties, e.g., in terms of mineral solubility, which could profoundly change dissolution-precipitation processes and their impact on CCS well integrity. This study presents the first reactive flow-through experiments performed using humid CO_2 as the flowing medium, allowing us to assess how the effective permeability of 2–20 μm wide casing-cement microannuli evolves under multiphase CO_2 reactive transport at 60 °C and 7–9 MPa pressure. After reference measurements using humid N_2, the results show that exposure to humid CO_2 can produce large reductions in defect effective permeability, with all samples reaching down to intact cement values. However, the overall reaction extent and amount of precipitation observed were limited compared to earlier flow experiments using carbonated brine. It is inferred that part of the observed reductions in flowrate likely occurred due to a shift in multiphase flow dynamics upon switching from humid N_2 to CO_2-based flow. Despite these differences, previously established self-sealing criteria for cement defects under carbonate brine flow seem to hold for humid CO_2 flow to within current experimental uncertainty.

1. Introduction

Carbon Capture and Storage (CCS) can minimize CO_2 emissions from industrial processes that are difficult to decarbonize and mitigate the climate impact of maintaining a reliable power supply throughout society's transition to sustainable energy sources (Linda and Singh, 2021; Mikunda et al., 2021; Procesi et al., 2013; Szulczewski et al., 2012). To avert emissions, CCS involves capture of CO_2 at large point sources, followed by its sequestration in a suitable storage complex. Given their large capacity, depleted hydrocarbon fields and deep saline aquifers are considered an attractive option (Belfroid et al., 2021; Godec

et al., 2011) but for such geological sequestration to be effective, storage permanence needs to be assured. Since wells must breach the natural seals provided by caprocks to gain access to subsurface formations, they form a well-known containment risk (Schimmel et al., 2019; Zhang and Bachu, 2011). Well designs must include artificial seals to safeguard zonal isolation, i.e., avert unwanted seepage of CO_2 along the wellbore. While bespoke sealants can be used for the construction of new wells, most legacy wells will contain pre-existing seals, which typically consist of steel casings surrounded and plugged by Portland cement.

Conventional Portland cements are well-known to react chemically with CO_2 (Carey, 2013; Choi et al., 2013; Jahanbakhsh et al., 2021;

Kutchko et al., 2007; Wolterbeek et al., 2013). The reactions occur when CO_2 dissolves in the porewater, leading to the formation and dissociation of carbonic acid:

$$CO_{2 \ (aq)} + H_2O_{\ (l)} \leftrightarrow H_2CO_{3 \ (aq)} \leftrightarrow H^+_{(aq)} + HCO^-_{3 \ (aq)} \leftrightarrow 2H^+_{(aq)} + CO^{2-}_{3 \ (aq)}$$
(R1)
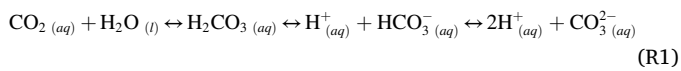
This acidification prompts the leaching or decalcification of alkaline compounds from the cement, such as portlandite and calcium silicate hydrate (C–S–H) phases, ultimately producing a silicate residue of relatively high porosity (Kutchko et al., 2007; Mason et al., 2014):

$$Ca(OH)_{2 \ (s)} \rightarrow Ca^+_{(aq)} + 2OH^-_{(aq)}$$
(R2)

$$\text{C-S-H}_{\ (s)} \rightarrow Ca^+_{(aq)} + OH^-_{(aq)} + SiO_{2 \ (am)}$$
(R3)
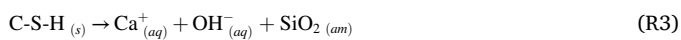
For moderate extents of CO_2 exposure, Reactions R2-R3 are able to effectively buffer the cement porewater pH to alkaline values, thereby producing carbonate ions via Reaction R1. Calcium liberated from the cement can then precipitate as calcium carbonate. These carbonates might redissolve upon excessive CO_2 exposure, however, i.e., if the cement pH buffering capacity gets depleted (Carey, 2013; Kutchko et al., 2007, 2008; Mason et al., 2013, 2014):

$$Ca^+_{(aq)} + CO^{2-}_{3 \ (aq)} \leftrightarrow CaCO_{3 \ (s)}$$
(R4)
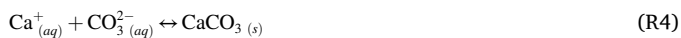
Together, Reactions R1-R4 produce a series of alteration zones. From the exposed surface into the cement interior, the following sequence is widely recognized in experiments using CO_2-rich brine: (Z1) a yellow-orange, porous, extensively reacted zone consisting of residual alumino-silicates, (Z2) an orange, tan to light-brown zone with mixed calcium carbonates, (Z3) a densely carbonated front, (Z4) a portlandite-depleted cement zone, and (Z5) unaffected cement (Hangx et al., 2016; Kutchko et al., 2007; Mason et al., 2013, 2014; Wigand et al., 2009). Zones Z2-Z5 have also been observed in CO_2-exposed wellbore cement recovered from downhole in-field studies (Carey et al., 2007; Duguid et al., 2014).

In intact cement, these alteration zones become wider as reaction advances further into the cement matrix. Due to the low matrix permeability of cement, the rate at which the fronts propagate is typically diffusion-controlled and very slow (Brunet et al., 2013; Duguid, 2009; Kutchko et al., 2008; Raoof et al., 2012). The reactions are therefore generally considered benign to low-permeability, tightly bonded cement seals over axial lengths relevant for well isolations, as it would easily take several tens if not hundreds of thousands of years for CO_2-rich brine to "eat its way through" a robust 50 m-long cement seal (Carey, 2013; Duguid, 2009; Zhang and Bachu, 2011). However, this situation could change drastically if permeable defects occur within the cement or along its boundaries with the steel casings or surrounding rock formations. Whether a result of issues during cement placement or setting (Barclay et al., 2001; Beltrán-Jiménez et al., 2022; Dusseault et al., 2000; Eslami et al., 2022; Roijmans et al., 2023; Wolterbeek et al., 2021a), or sustained from thermo-mechanical loads during subsequent operations (Dou et al., 2020; Gu et al., 2017; Lecampion et al., 2013; Orlic, 2009; Wolterbeek and Hangx, 2023; Wolterbeek et al., 2016a), casing-cement microannuli and other flaws may provide permeable pathways (Moghadam et al., 2022; Wolterbeek et al., 2021b). If such defects allow large volumes of CO_2 to infiltrate and react with the sealant materials under advective flow conditions, then reaction could aggravate or alleviate seepage over time.

Given the possible ramifications for zonal isolation integrity, numerous studies have investigated how the inflow of CO_2 and associated chemical alteration affect the permeability of cracked cement (Abdoulghafour et al., 2013, 2016; Cao et al., 2015; Huerta et al., 2013, 2016; Liteanu and Spiers, 2011; Luquot et al., 2013; Miao et al., 2022; Nguyen et al., 2020) and microannuli along debonded cement-casing interfaces (Carey et al., 2010; Wolterbeek et al., 2016b, 2019). These experiments are interesting, as some show stable or even mildly enhancing seepage, while others show strongly self-limiting flow due to defect clogging by mineral precipitation. Numerical modelling studies of the underlying reactive transport processes show that these diverging lab observations can be largely reconciled as the result of a competition between dissolution-leaching of cement phases and carbonate precipitation-dissolution (Ajayi and Gupta, 2019; Brunet et al., 2016; Cao et al., 2015; Guthrie et al., 2018; Iyer et al., 2017, 2018; Wolterbeek and Raoof, 2018). Based on these models, the conditions for self-sealing versus non-sealing CO_2 reactive transport can be defined in terms of the i) initial defect aperture and ii) fluid residence time (Brunet et al., 2016; Iyer et al., 2017, 2018). In essence, narrower defects are easier to seal off and longer interaction times allow for more mineral precipitation. Validated against experiments, the models provide tools for upscaling and evaluation of wellbore integrity in CCS complexes, where small defects in the cement seem to possess some capacity to self-seal against CO_2.

It must be emphasized, however, that all reactive flow-through experiments performed on cement to date have involved exposure to single-phase flow of CO_2-rich aqueous fluids (i.e., water or brine with dissolved CO_2). This choice made practical sense, since water-based, single-phase flow measurements are easier to setup and interpret, and such lab results are also easier to model in the context of aqueous fluid chemistry. However, water-based flows are not very representative for field situations, as seepage along real wells is more complex (Feng et al., 2017; Iyer et al., 2018; Kjøller et al., 2016; Wolterbeek et al., 2019). Due to the incomplete miscibility and stark density contrast between CO_2 and aqueous brines – 270–770 kg m^{-3} vs. 940–1230 kg m^{-3} under typical reservoir conditions (Emami-Meybodi et al., 2015) – buoyancy forces will cause the injected CO_2 to migrate upwards within the storage formation until it reaches and collects underneath a structural trap provided by caprock (Fig. 1a). While the CO_2 will partially dissolve in resident formation brine, the resulting CO_2-rich aqueous fluid is relatively dense and anticipated to migrate downward along the base of the storage formation (Fig. 1a). Instead of carbonated brine, it is therefore much more likely that wellbore seepage will involve mainly humid CO_2 flow (in its gaseous, liquid, or supercritical state) or possibly multiphase flow of CO_2- and water-rich fluids (Feng et al., 2017; Iyer et al., 2018).

The fluid properties of humid CO_2 are very different from those of CO_2-rich brine, e.g., in terms of mineral solubility. In batch reaction experiments on cement (i.e., without flow), humid CO_2 and CO_2-rich water are known to produce distinct alteration patterns (Kutchko et al., 2011; Wolterbeek et al., 2013). Under flow conditions, fluid-fluid interactions between the humid CO_2 and porewater can cause capillary effects, buoyancy-driven flows, and transient flow paths (Dusseault and Jackson, 2014; Gorody, 2012; Lecampion et al., 2013; Rice et al., 2018). Such multiphase flow phenomena may profoundly impact reactive transport. Note Reactions R1-R4 all occur in an aqueous fluid phase. Flow of humid CO_2 (a non-aqueous fluid) instead of carbonated brine will drastically reduce the mobility of water-soluble species in the defect and may change interactions with porewater inside the cement matrix. This will undoubtedly impact ionic transport and hence the amount and distribution of dissolution and precipitation. This may be beneficial, as excessive leaching and cement degradation become much less likely if there is limited water in which carbonates can dissolve. On the other hand, precipitation clogging may also become less efficient (Wolterbeek and Hangx, 2021). In a numerical modelling study of possible two-phase flow effects, Iyer et al. (2018) found that the self-sealing processes may slow down or even fail to achieve defect closure if reactive surface area reduces with decreasing water saturation. Unfortunately, the impact of CO_2-dominated multiphase reactive flow on defects in cement has received little attention experimentally, leaving these aspects poorly understood.

In this study, we present the first reactive flow-through experiments performed using humid CO_2 as the main flowing medium instead of carbonated brine. Tests were performed on 30 cm-long cemented casing samples bearing 2–20 μm wide interfacial microannuli. The results
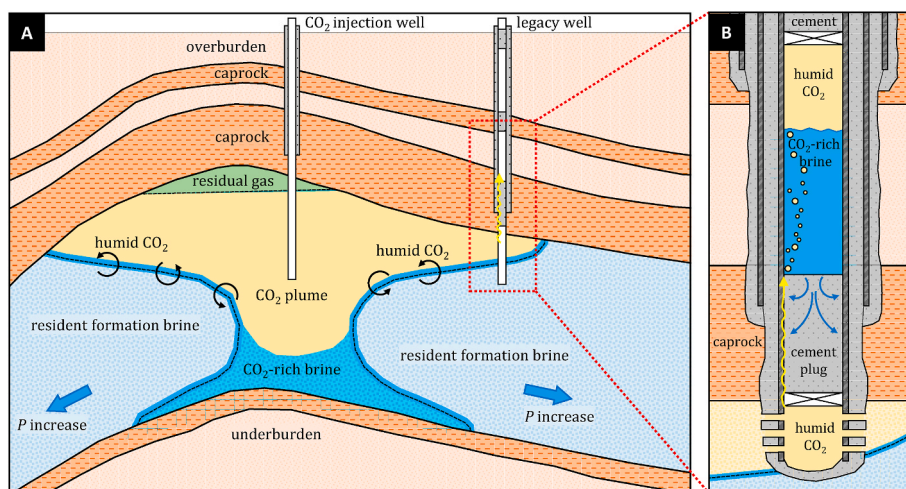
Fig. 1. Wellbore seepage scenario envisioned in the present study (drawings not to scale); a) depleted gas reservoir repurposed for geological storage of CO_2, consisting of a storage formation (blue) overlain by caprock (orange), containing residual natural gas (green) and injected CO_2 (yellow); and b) diagram illustrating the primary features of a cemented and plugged legacy wellbore, including humid CO_2 seepage, carbonation of water-based well completion fluids, and the formation of a CO_2-based "gas cap" below the next cement plug. Following injection, the CO_2 plume (yellow) migrates upward through the reservoir due to buoyancy forces until it reaches the impermeable caprock. For this reason, fluid migration along legacy wellbores may involve predominantly humid CO_2 rather than CO_2-rich brine.

obtained allow us to assess whether or not the self-sealing effects previously observed in cement defects during seepage of CO_2-rich brine will also occur in the more likely field scenario of seepage of humid CO_2 along cemented CCS wells. To this end, we interpret our data in the context of multiphase flow patterns, relative permeability effects, fluid residence times, and cement reactive self-sealing ability.

2. Experimental procedures

2.1. Simulated well seepage scenario

This study reports CO_2 flow-through experiments (60 °C, 7–9 MPa fluid pressure) on cement-plugged steel pipes containing 2–20 μm wide casing-cement microannuli. The applied temperature and pressure are considered representative for downhole well conditions at roughly 1–2 km depth, and were also selected to enable comparisons with previous research. The envisioned seepage scenario consists of a legacy well, located some distance away from the CO_2 injection point in a repurposed gas reservoir (Fig. 1a). This well suffers only minor defects like microannuli, assuming larger issues were noticed and addressed upon abandonment. Still, microannuli may have sustained difficult-to-detect levels of natural gas seepage for years, changing the saturation and distribution of water inside the defects prior to arrival of the CO_2 plume. Water displaced from the microannuli likely accumulated atop the cement seals, where flow velocities drop due to widening of the flow path (Fig. 1b). In our experiments, this preconditioning due to natural gas seepage was simulated using humid N_2 flow, imposed over initially waterlogged cement plugs. The N_2 stage was continued until a quasi-steady state was attained. At this point, the microannuli were presumably filled largely with N_2, while the cement matrix likely retained its porewater by virtue of high capillary entry pressure thresholds (Slowik et al., 2008). As the injection plume reaches the legacy well in our scenario, natural gas can get replaced by CO_2 as the seepage fluid. In our experiments, we initiated this stage by switching from humid N_2 to CO_2 flow, monitoring for changes in transport properties over time.

2.2. Materials and sample preparation

Experiments were performed on 30 cm-long cement-plugged pipes with 2–20 μm wide microannuli along their steel-cement interfaces. Samples were made from ASTM A106 Grade B steel seamless pipe (60.3

mm outer diameter, 49.2 mm inner diameter) using equipment described by van Eijden et al. (2017). The pipes were fitted with bottom caps containing an adjustable base. Slurries were prepared from API Class G HSR Portland cement at a water-to-cement (w:c) mass ratio of 0.44 and mixed per API RP 10B-2 (2013). After gently placing 700 ml slurry topped with 10 ml water inside, the pipes were connected vertically to a pressurization system (see Fig. 5 of van Eijden et al., 2017). The cement was allowed to cure for 3 weeks at 60 °C under 5 MPa N_2. After unmounting and replacing the endcaps with plastic seals, the wet cemented pipes were stored at room temperature until use. All samples naturally contained microannuli, providing initial permeability. In addition, Samples A and B were compressed laterally using a press, slightly flattening the pipe to create fractures and increase initial permeability. For each experiment, the plastic seals used to contain fluids during storage were removed, after which ~10 ml of water was placed on top of the cement plug. The cemented pipe was then closed off using Hastelloy endcaps and mounted vertically in the flow-through setup (Fig. 2).

2.3. Reactive flow-through setup

2.3.1. Permeameter system

Experiments were performed in a reactive flow-through facility capable of subjecting samples to inflow of humid CO_2 and CO_2-rich aqueous solutions under downhole conditions (up to 120 °C and 11 MPa). The permeameter consisted of two Vindum VP-3K-HT high pressure pumps and two Endress + Hauser Proline Promass A 500 Coriolis meters, connected to the upstream (US) and downstream (DS) ends of the sample (Fig. 2). The US and DS pumps were operated in continuous flow, constant pressure mode, such that together they maintained a fixed differential pressure across the sample (measured independently using a Yokogawa EJA110E-JVA5G-914EN pressure transmitter; denoted DPT). The US and DS parts of the setup could be disconnected using a separator tap (Fig. 2), forcing all flow through the sample. Prior to closing this tap, a short circuit allowed the entire system to be pressurized evenly. Coriolis meters were used to monitor the density and flowrate of influent and effluent fluids. Flow was imposed against gravity, i.e., the bottom of the cement plug corresponds to the US side. The US pump was connected to a reactor vessel, used to source humid N_2 and CO_2 (Section 2.2.2). The permeameter and reactor vessel were maintained at 60 °C in an oven. Influent fluid temperature was measured
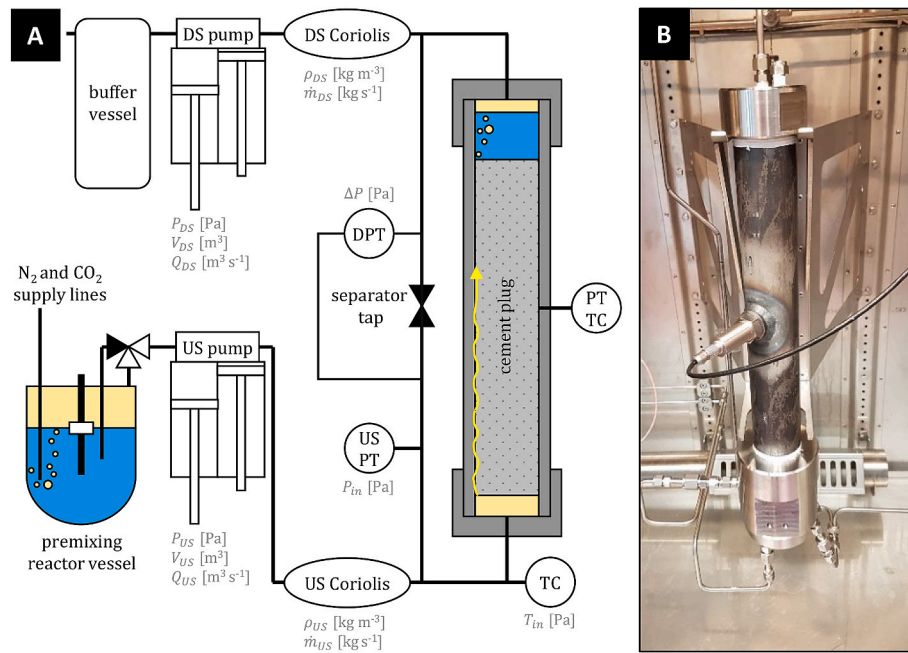
Fig. 2. Overview of the Shell CCS Zonal Isolation Unit, with a) simplified schematic showing the main features of the setup, with various measurements indicated in grey, and b) photograph of a mounted sample assembly inside the oven. Symbols and acronyms are defined in Sections 2.2 and 2.4. Note the lateral pressure transducer, visible on both the schematic and photo, was not used in the current experiments.

inline.

2.3.2. The N_2–CO_2–H_2O fluid source system

Humid N_2 and CO_2 were prepared in a reactor vessel (10 l) equipped with ESI Technology HI2300-0120AM pressure transmitter (PT), TC Direct 12N-LTS-156-1.5-2I thermocouple (TC), and Magnetrol 706-512C–B11 Guided wave TDR level transmitter (Fig. 2). Before each test, this vessel was filled with 7 l deionized water. Pressurized N_2 or CO_2 was bubbled through the water via a submerged inlet, both before and during active flow measurement. The vessel would first be equilibrated with N_2 at 60 °C and 6.5 MPa total pressure, resulting in a "gas cap" of humid N_2 above the water. The reactor was equipped with two outlets, one each for sampling from the top and bottom of the vessel. Here, the upper outlet was used to deliver humid N_2 to the US pump. Pressure was sustained by simultaneously supplying dry N_2 to the reactor via the submerged inlet, while the level indicator ensured enough water remained for effective humidification. The same reactor and procedures were used to source humid CO_2 later on.

2.4. Testing procedure

The experiments involved two stages. The cemented pipes were first exposed to humid N_2 flow. This stage served to precondition the sample (i.e., ensure fully developed gas-water multiphase flow conditions) and determine the initial effective permeability. The samples were subsequently subjected to humid CO_2 flow, monitoring flowrate and fluid composition under fixed pressure difference conditions. For the first stage, the setup was pressurized to 7 MPa using humid N_2 with the separator tap open. After awaiting thermal stability and checking for leaks, the separator tap was closed. Humid N_2 flow was then initiated by increasing pressure in the US pump and continued until a quasi-steady state was attained. At this point, the microannuli were presumably filled largely with humid N_2 while the cement will have retained much of its porewater by virtue of the high capillary entry pressures required to invade its matrix porosity (Slowik et al., 2008). Flowrates recorded in this stage provided a measure for the samples' initial effective permeability.

The switch from humid N_2 to humid CO_2 flow was achieved either immediately or gradually. To perform an "immediate switch", flow was briefly arrested by closing off the US pump. Subsequently, the reactor vessel was vented to remove the N_2 and then refilled with CO_2 at 6.5 MPa. After allowing the CO_2–H_2O mixture to settle, flow would be reinitiated by reconnecting the US pump. The advantage of this method is that it produces a relatively sharp transition from humid N_2 to CO_2 flow. The downside of this approach is that flow was interrupted, potentially disturbing the multiphase flow pattern. To avoid such effects, two tests employed a "gradual switch" instead. Here, the gas feed to the reactor vessel was changed without venting, leaving the US pump operational to achieve uninterrupted flow-through conditions. Consequently, the influent fluid changed only gradually from humid N_2 to humid CO_2, as mixing in the reactor vessel produced a humid [N_2+CO_2] phase. Changes in the influent and effluent fluid composition were monitored continuously and inline using the Coriolis meters. The CO_2-based flow stage was continued for up to 1000 h. In some experiments, the applied pressure difference was changed in steps, e.g., if flowrates started to fall below practical measurement limits.

Note small changes in specific procedures of the different flow-through experiments allowed us to assess the impact of defect geometry and flow history. In addition to casing-cement microannuli, Samples A and B were made to contain internal cracks in the cement plug. In Sample C, we chose to impose pressure steps during the humid nitrogen flow stage to investigate drainage and relative permeability effects. Since the size of the microannuli that formed during sample preparation proved variable and difficult to control, the imposed differential pressure was adjusted from test to test in order to obtain stable flow in the setup.

2.5. Data acquisition and processing

LabView-based software was used to log data every 5 s, including the: i) cumulative pumped volume of the US and DS pumps, V_{US} and V_{DS} [m^3], ii) pump flowrates, Q_{US} and Q_{DS} [m^3 s^{-1}], iii) pump pressures, P_{US} and P_{DS} [Pa], iv) Coriolis-based influent and effluent fluid densities, ρ_{US} and ρ_{DS} [kg m^{-3}], v) Coriolis-based flowrates, $\dot{m}_{US}$ and $\dot{m}_{DS}$ [kg s^{-1}], vi)

differential pressure acting across the sample, ΔP [Pa], vii) pressure at the inlet of the sample, P_{in} [Pa], and viii) influent fluid and oven temperature, T_{in} and T_{oven} [°C]. Logged data were processed to obtain the effective gas permeability of the cement-plugged pipes, κ_{eff} [m^2], using a Darcy flow relation for compressible fluids:

$$\kappa_{eff} = \frac{\overline{\mu}\overline{z}RT}{M} \frac{\dot{m}}{A} \frac{2L}{\left(P_{in}^2 - P_{out}^2\right)} \qquad (1)$$

Here, $\overline{\mu}$ [Pa s], $\overline{z}$ [-], and M [kg mol^{-1}] are the dynamic viscosity at mean pressure, compressibility factor at mean pressure, and molar mass of the fluid, respectively; R [J K^{-1} mol^{-1}] is the gas constant, T [K] denotes temperature, $\dot{m}$ [kg s^{-1}] is the mass flowrate, L [m] and A [m^2] are plug length and cross-section, and P_{in} and P_{out} [Pa] are the sample inlet and outlet pressure (note $P_{out} = P_{in} - \Delta P$). Influent and effluent fluid compositions were estimated from the measured density, pressure and temperature. Fluid properties were subsequently derived from reference data for N_2 and CO_2 from the NIST Chemistry Webbook, SRD 69 (Lemmon et al., 2016). More detailed methods, including a derivation of Equation (1) and a discussion of the steps and assumptions involved in data processing can be found in the Supporting Information.

2.6. Post-experiment microstructural and chemical analysis

After completion of the experiments, the cement-plugged pipes were subjected to microstructural analysis. Samples were cooled and depressurized slowly before removal from the permeameter. After water on top of the plugs was gently poured out, the samples were inspected visually. Subsequently, sections through the pipe, oriented perpendicular to the overall flow direction, were created every ~4 cm along the length of the plugs. Selected sections were studied using reflected light microscopy to observe the microstructure and micro-X-ray fluorescence (µXRF) analysis to map chemical zonation.

3. Results and analysis

Key data obtained in the four reactive flow-through experiments performed in this study are summarized in Table 1. The permeability results and microstructural observations are described below.

3.1. Flow history and permeability evolution

Since cement has a low matrix permeability (10^{-21} to 10^{-17} m^2 –Nelson and Guillot, 2006; Taylor, 1997), gas flow through the samples is expected to have occurred mainly via the defects created during sample preparation. Despite post-test microstructural study, these defects' in-situ geometry is challenging to constrain and may have evolved during flow. The samples' transport properties will therefore be presented in terms of their effective gas permeability, κ_{eff} [m^2], calculated relative to the pipe cross-section ($A = \pi r_{tube}^2$ [m^2]). Presented data thus include possible contributions from i) changes in defect geometry, e.g., due to dissolution-precipitation reactions, ii) relative permeability effects, and iii) elastic deformation of the pipe. Note volume flowrates and injected volumes are reported at in-situ pressure-temperature conditions.

3.1.1. Sample A

Humid N_2 flow in Sample A was initiated at $\Delta P = 0.4$ MPa. The resulting mass flowrate slowly increased from 56 to 63 g h^{-1} over the first 20 h. As expected, fluid densities approached reference values for N_2. The initial κ_{eff} measured $2.2 \cdot 10^{-15}$ m^2 (Fig. 3). About 16 l of humid N_2 was injected during preconditioning. At this point, flow was arrested for 15 min to make an "immediate switch" from N_2 to CO_2 (Section 2.4). Upon reinitiating flow ($\Delta P = 0.4$ MPa), the influent volume flowrate measured 550 ml h^{-1}, while the influent fluid density increased sharply as CO_2 replaced N_2. This caused the influent mass flowrate to reach 92 g

Table 1
Overview of experimental data and calculated properties. All of the experiments were performed at 60 °C and a downstream fluid pressure of 7 MPa. *See Section 3.3 for definitions and relevant equations.

Properties	Sample A	Sample B	Sample C	Sample D
initial pressure difference (ΔP at $t = 0$) [MPa]	0.4	0.2	0.8	0.2
maximum applied pressure difference [MPa]	1.2	0.2	1.6	1.0
initial fluid flow rate (Q at $t = 0$) [ml h^{-1}]	800–900	260–330	180–210	130–180
cement plug length (L) [cm]	33.3	34.6	32.0	33.4
initial apparent permeability (κ at $t = 0$) [m^2]	$2.2 \cdot 10^{-15}$	$1.6 \cdot 10^{-15}$	$2.5 \cdot 10^{-16}$	$9.0 \cdot 10^{-16}$
final apparent permeability [m^2]	~$5 \cdot 10^{-18}$	~$3 \cdot 10^{-17}$	~$7 \cdot 10^{-19}$	~$1 \cdot 10^{-17}$
defect aperture*:				
- initial flow-based estimate (w_H) [µm]	~7	~6	~3	~5
- final microstructure-based estimate (w_M) [µm]	0–20	0–20	0–5	0–15
defect void volume*:				
- hydraulic aperture-based estimate (V_{aH}) [cm^3]	0.35	0.32	0.16	0.26
- microstructure-based estimate (V_{aM}) [cm^3]	1.02	1.06	0.25	1.03
fluid residence time*:				
- hydraulic aperture-based estimate (τ_{QH}) [s]	~2	~4	~3	~7
- microstructure-based estimate (τ_{QM}) [s]	~5	~15	~5	~21
- fluid density-based estimate (τ_D) [h]	~1	~3	~6	~12
observed defect types in microstructures [-]	microannuli + large cracks	microannuli + minor cracks	microannuli + minor cracks	microannuli

h^{-1} in 15 min (Fig. S2). During this period, the effluent volume flowrate was similar (~600 ml h^{-1}), while effluent density and mass flowrate remained lower (40–45 g h^{-1}). Note the flowrates immediately after switching are slightly lower than those at the end of N_2-based testing, which may reflect changes in relative permeability due to temporary cessation of flow during the switchover.

Influent density leveled off at 165 kg m^{-3} about 15 min after starting CO_2-based flow. Roughly concurrently, flowrates began to decrease, reducing one order of magnitude in 30 min. Effluent fluid density started to increase after 45 min, signaling CO_2 breakthrough. The initial drop in κ_{eff} was followed by a more gradual decrease, reaching another order of magnitude reduction in 50 h. Due to a small leak in the permeameter, the influent and effluent flowrates began to deviate as they decreased. Beyond 40 h, the leak outstripped flow through the sample, prompting the DS pump to reintroduce previously expelled N_2 to maintain pressure. After 95 h, the US pressure was increased to 7.8 MPa and later to 8.2
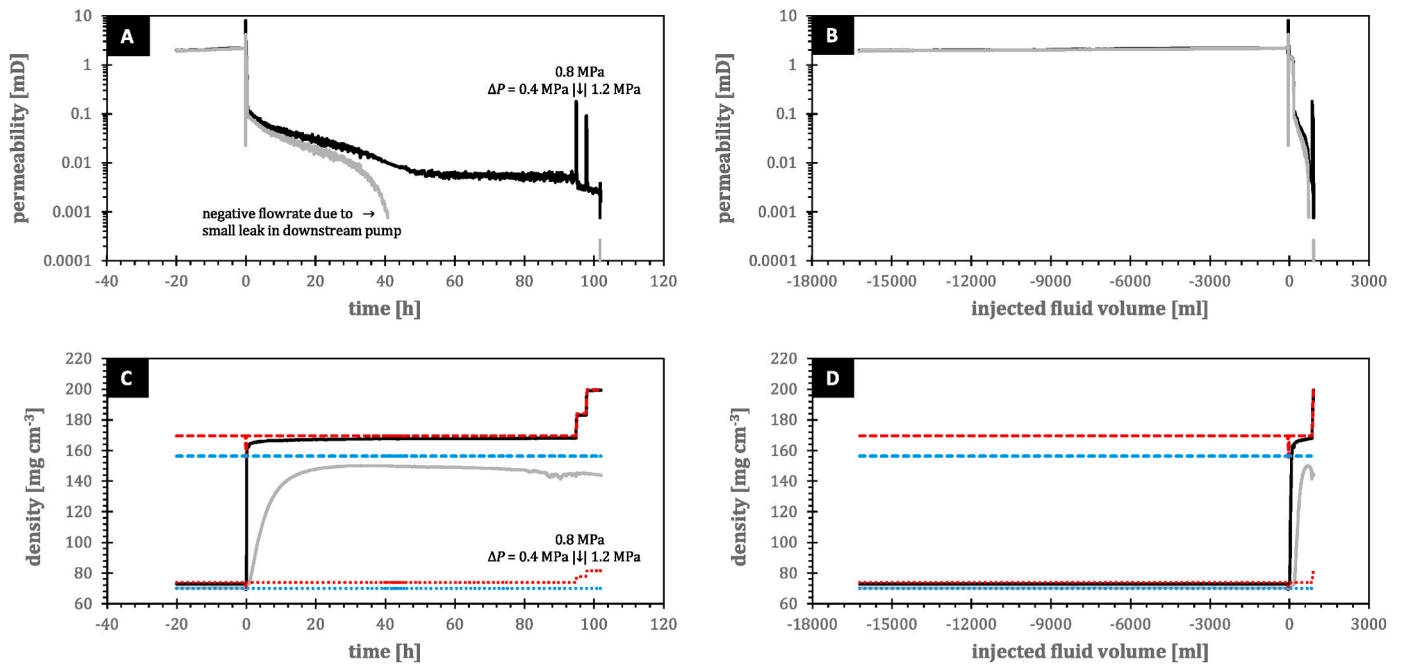
Fig. 3. Reactive flow-through results for Sample A, with a-b) effective gas permeability [m^2] and c-d) fluid density [kg m^{-3}] versus time [h] and injected fluid volume [ml], respectively. Black and grey data represent US and DS pump measurements, respectively. Zero run time and zero injected volume are defined at the moment flow using CO_2-based fluid was initiated. The N_2-based permeametry results therefore plot in the negative time and volume domains. Reference densities for pure CO_2 and N_2 are plotted as dashed and dotted lines, respectively. Reference densities at US and DS pressure are plotted in red and blue, respectively.

MPa, such that ΔP doubled and tripled. Aside from small transient effects, this did not impact κ_{eff}, which remained below $1 \cdot 10^{-17}$ m^2, i.e., over two orders of magnitude lower than the initial permeability and satisfying industry requirements for "good quality cement" isolations (e. g., below 35 µD; OEUK, 2022). The experiment was terminated after 102 h of reactive flow, injecting 900 ml of humid CO_2.

3.1.2. Sample B

The initial κ_{eff} of Sample B measured $1.6 \cdot 10^{-15}$ m^2 (Fig. 4). During N_2 flow at $\Delta P = 0.22$ MPa, flowrates increased slowly from 19 to 24 g h^{-1}, reaching stable values beyond 14 h. Overall, the preconditioning stage involved injection of 5.7 l of humid N_2. The gas feed to the reactor vessel was then changed from N_2 to CO_2 without arresting flow, so that the transition to humid CO_2 occurred more gradually than in Sample A
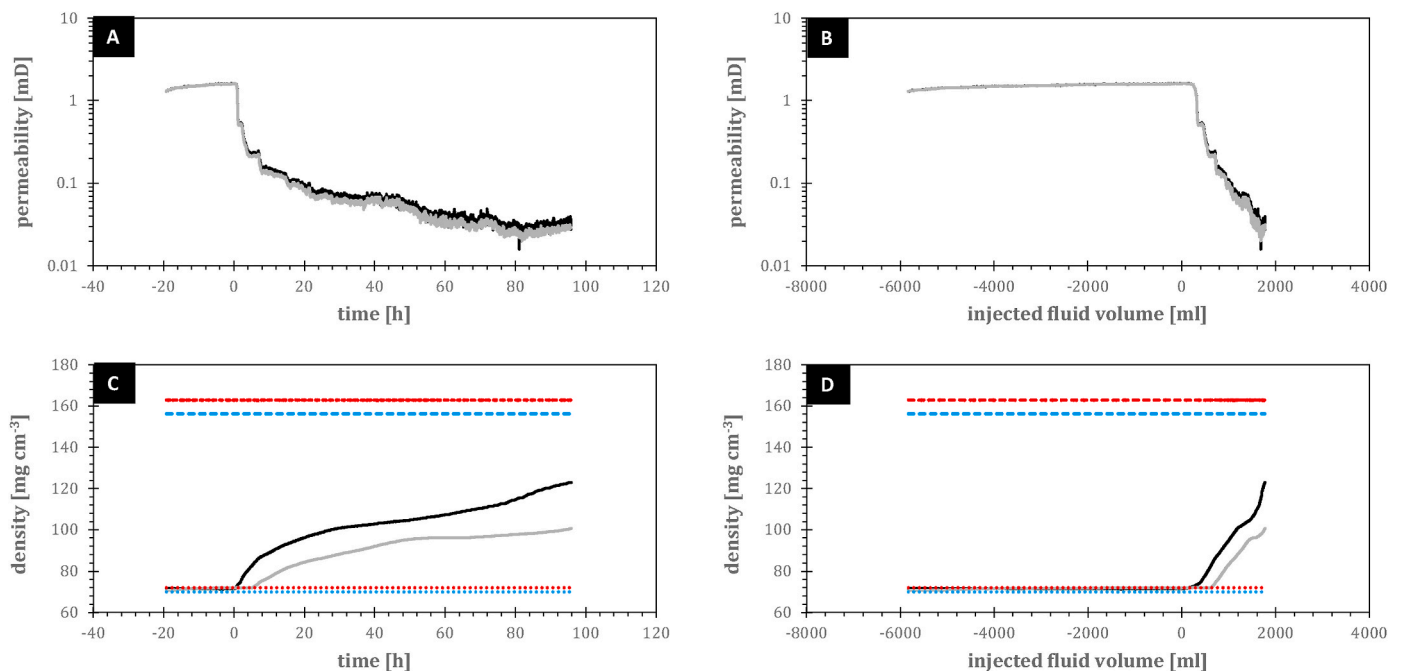

Fig. 4. Reactive flow-through results for Sample B, with a-b) effective gas permeability [m^2] and c-d) fluid density [kg m^{-3}] versus time [h] and injected fluid volume [ml]. Black and grey data represent US and DS pump measurements, respectively. Zero run time and zero injected volume are defined at the moment flow using CO_2-based fluid was initiated. The N_2-based permeametry results therefore plot in the negative time and volume domains. Reference densities for pure CO_2 and N_2 are plotted as dashed and dotted lines, respectively. Reference densities at US and DS pressure are plotted in red and blue, respectively.
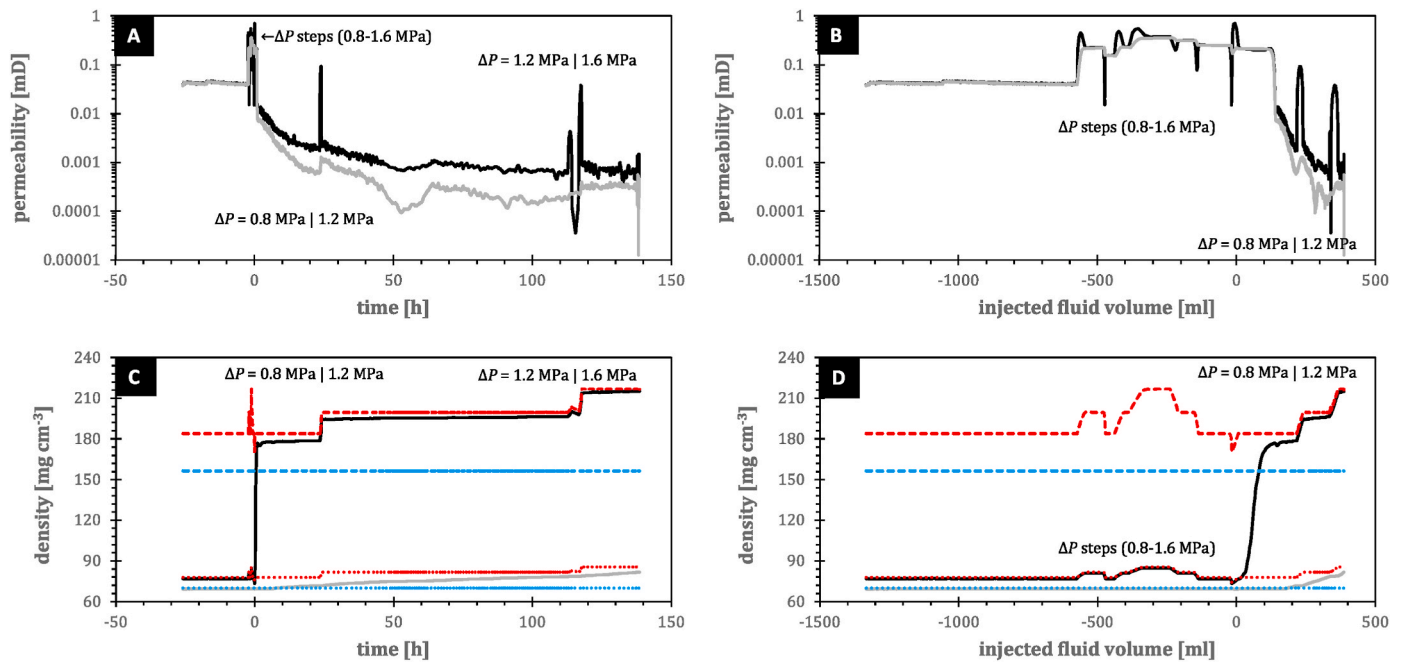
Fig. 5. Reactive flow-through results for Sample C, with a-b) effective gas permeability [m^2] and c-d) fluid density [kg m^{-3}] versus time [h] and injected fluid volume [ml]. Black and grey data represent US and DS pump measurements, respectively. Zero run time and zero injected volume are defined at the moment flow using CO_2-based fluid was initiated. The N_2-based permeametry results therefore plot in the negative time and volume domains. Reference densities for pure CO_2 and N_2 are plotted as dashed and dotted lines, respectively. Reference densities at US and DS pressure are plotted in red and blue, respectively.

(Section 2.4). Influent density started to increase after injection of 200 ml [N_2+CO_2] fluid, signaling rising CO_2 concentrations at the inlet. Near concurrently, flowrates decreased from 330 to 100 ml h^{-1} after 30 min. CO_2 breakthrough occurred 5 h after switching the gas feed, producing a sharp increase in effluent density. Beyond this point, both influent and effluent density increased steadily. Following its initial drop, κ_{eff} continued to reduce in steps, with flowrates reaching 25 ml h^{-1} after 10 h. This decreasing trend in κ_{eff} persisted, albeit more gradually, with flowrates reducing to 6 ml h^{-1} after 95 h. At this point, a power failure caused premature experiment termination. The final κ_{eff} measured $\sim$3·10^{-17} m^2, a factor 50 lower than the initial permeability. Overall, reactive flow testing on Sample B involved injection of 1.7 l of humid [N_2+CO_2] fluid at ΔP = 0.22 MPa.

3.1.3. Sample C

Sample C was characterized by a lower initial κ_{eff}. Application of ΔP = 0.8 MPa yielded a N_2 flowrate of 34 ml h^{-1}. Before switching to CO_2 flow testing, Sample C was used to assess pressure history effects. This was done by varying ΔP between 0.8 and 1.6 MPa (Fig. 5). Upon increasing ΔP from 0.8 to 1.2 MPa, effluent flowrate rose from 35 to 250 ml h^{-1}. Subsequently decreasing ΔP back to 0.8 MPa resulted in a flowrate of 120 ml h^{-1}, demonstrating that temporary increases in ΔP produce irreversible changes in κ_{eff}. Increasing ΔP to 1.2 MPa again, and then further to 1.6 MPa, yielded flowrates of 260 ml h^{-1} and 550 ml h^{-1}, respectively. Subsequently returning to ΔP = 0.8 MPa resulted in an effluent flowrate of 213 ml h^{-1}, which then remained stable during injection of 120 ml. This corresponds to an initial κ_{eff} of 2.5·10^{-16} m^2. Overall, preconditioning and reference measurements involved injection of 1.3 l of humid N_2. At this point, flow was briefly interrupted to switch fluids, following procedures as for Sample A.

Upon reinitiating flow using CO_2, effluent flowrate recovered to 180 ml h^{-1}. Influent density increased rapidly, reaching 177 kg m^{-3} within 1 h before stagnating slightly below CO_2 reference values. Concurrently, flowrates decreased by over one order of magnitude. After 7 h and injection of 200 ml, the effluent density slowly began to increase above reference values for N_2, indicating CO_2 breakthrough. The κ_{eff} continued

to drop steadily, with influent and effluent flowrate reducing to 1.4 ml h^{-1} and 0.5 ml h^{-1} in 24 h, respectively. At this stage, ΔP was increased to 1.2 MPa. This resulted in a temporary increase in flowrate, but the overall trend remained one of reducing flow over time. After 112 h of CO_2 flow, ΔP was raised to 1.6 MPa, again resulting in transiently higher flowrates. After 138 h and injection of 386 ml fluid, the CO_2 flow stage was ended. Final κ_{eff} ranged 2·10^{-19} to 7·10^{-19} m^2, which corresponds to roughly three orders of magnitude reduction and is on par with cement matrix permeabilities (Nelson and Guillot, 2006; Taylor, 1997).

3.1.4. Sample D

Measurements on Sample D were initiated at ΔP = 0.2 MPa (Fig. 6). The resultant flow slowly increased from 130 to 175 ml h^{-1} (9–13 g h^{-1}) in 70 h, while injecting $\sim$10 l of N_2. This corresponds to an initial κ_{eff} of 9·10^{-16} m^2, with Sample D thus falling in between the other samples tested. Changeover to CO_2-based flow was done gradually, as for Sample B. Around t = 1 h (after 100 ml inflow), injection of humid [N_2+CO_2] started to raise the influent density. About 30 min later, a response in flowrate was registered, which reduced from 175 ml h^{-1} to below 60 ml h^{-1} (4 g h^{-1}) in 1 h. This initial drop was followed by a more gradual reduction in κ_{eff}, with flowrates decreasing to below 20 ml h^{-1} in 10 h. Effluent fluid density began to exceed N_2 reference values after 15 h, indicating CO_2 breakthrough. These trends of increasing fluid density and decreasing flowrate persisted over 550 h of flow at ΔP = 0.2 MPa. Overall, κ_{eff} lowered to 1·10^{-18}-5·10^{-18} m^2, reaching two-three orders of magnitude reduction and attaining cement matrix values.

On top of the overall increasing trend in fluid density, Sample D showed episodes of transiently elevated density (Fig. 6). These "bumps" were most pronounced in the effluent fluid but also visible in the influent fluid. Note the features directly preceded periods where flowrate attained its lowest values, corresponding to κ_{eff} well below 5·10^{-19} m^2. After 550 h, ΔP was increased to 1 MPa. This caused the flowrate to jump from less than 0.1 g h^{-1} to 7 g h^{-1} (40 ml h^{-1}), roughly corresponding to a κ_{eff} of 3·10^{-17} m^2. Effluent fluid density also increased rapidly, reaching CO_2 reference values in 10 h. During the next 190 h, flowrates gradually reduced to 6 g h^{-1}. Influent and effluent fluid
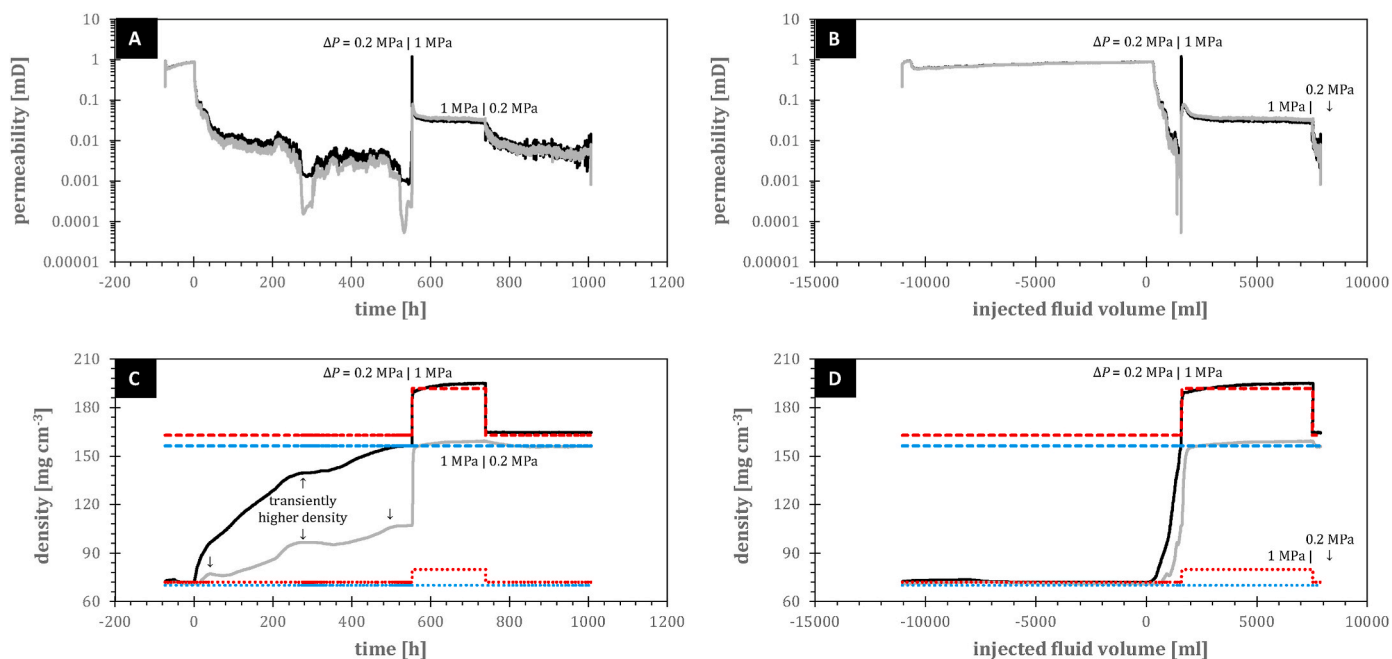
Fig. 6. Reactive flow-through results for Sample D, with a-b) effective gas permeability [m^2] and c-d) fluid density [kg m^{-3}] versus time [h] and injected fluid volume [ml]. Black and grey data represent US and DS pump measurements, respectively. Zero run time and zero injected volume are defined at the moment flow using CO$_2$-based fluid was initiated. The N$_2$-based permeametry results therefore plot in the negative time and volume domains. Reference densities for pure CO$_2$ and N$_2$ are plotted as dashed and dotted lines, respectively. Reference densities at US and DS pressure are plotted in red and blue, respectively. See main text for discussion on the transiently higher densities observed in this experiment; note these periods correspond to lows in effective permeability.

density continued to increase, noticeably exceeding CO$_2$ reference values at 600 h. These high densities likely reflect added mass from water droplets entrained in the flow, i.e., water-<u>over</u>saturated [N$_2$+CO$_2$] fluid. The density bumps observed earlier in the experiment may also reflect entrainment effects. After 738 h, ΔP was returned to 0.2 MPa. This immediately resulted in an order of magnitude reduction in flow-rate, followed by a more gradual decrease towards ~1 ml h^{-1}. The influent and effluent fluid density decreased to CO$_2$ reference values (note this took over a day for the effluent fluid, which may reflect liquid holdup in the Coriolis meter). The experiment was terminated after 1008 h and injection of 7.9 l of CO$_2$-based fluid. At this time, κ_{eff} of Sample D measured ~1·10^{-17} m^2.

3.2. Microstructural and mineralogical observations

Upon retrieval, all samples still had liquid water on top of the cement plugs, while the cement bottom ends generally appeared damp to partially dried (note the bottom is the US side with respect to flow). The cement at the bottom end was generally brownish grey in color, whereas the submerged cement at the top of the plugs was orange brownish, sometimes partially covered in white precipitates. The inner wall of the steel pipe, insofar as free of cement, was dark brownish and appeared stained. As the pipes contained a mill varnish, it was challenging to assess corrosion scale formation on the steel.

Cross-sections created perpendicular to the steel pipe axis, i.e., overall flow direction, revealed the post-experiment condition of the cement plugs, including the defect architecture and chemical zonation. Fig. 7 shows reflected light images of sections of Sample B, also indicating areas where detailed photographs and μXRF element maps were obtained (Fig. 8). Additional microstructure images of the three other samples are provided in the Supporting Information (Figs. S6–S10). In the following, we will first consider the geometry and interconnectedness of the defects and subsequently describe the chemical alteration patterns observed.

3.2.1. Defect geometry

All four samples contained debonding defects along their steel-cement interfaces. Insofar assessable from the cross-sections, the microannuli appeared relatively constant along both the circumference and length of the plugs. The cement further contained tensile cracks and other small flaws, oriented roughly parallel to the pipe axis (note fractures were created on purpose in Samples A and B). Obtaining quantitative measurements of the defects proved challenging due to their small size, obscuring effects from chemical alteration, and concealment due to smearing of the steel pipe during cutting and polishing. All four samples also contained up to mm-size, spherical voids in the cement. These macropores likely originated as small water droplets, created due to imperfect mixing and subsequently trapped during cement curing.

In Sample A, interfacial debonding was slightly asymmetric, with microannulus apertures varying along the pipe circumference from indiscernibly thin to 20 μm. Sample A further contained two sets of cracks of roughly perpendicular orientations (Fig. S6). The cracks were obscured by alteration but estimated 2–20 μm wide. The defect geometry of Sample A remained fairly constant along the cement plug but axial interconnectedness of the internal cracks was hard to determine. Sample B showed a broadly similar defect geometry, with a micro-annulus of up to 20 μm wide. A section made halfway the plug showed a hairline fracture with signs of chemical alteration, but the preceding and succeeding sections both appeared free of fractures (Fig. 7). The downstream-most section showed more extensive fractures again, but here the bordering cement lacked any signs of alteration, suggesting these fractures are unlikely to have supported flow during the reactive flow stage or may even represent post-test features. In Sample C, the microannulus did not exceed ~5 μm and was difficult to discern (Fig. S7). Hairline fractures bordered by very faint alteration zones occurred roughly halfway the cement plug but were not observed in the other sections. The defect geometry of Sample D closely resembled the others, with a debonding microannulus along the cement-steel interface of up to ~15 μm wide (Fig. S8). The downstream-most section contained some internal fractures, but these did not show chemical alteration of the adjacent cement.
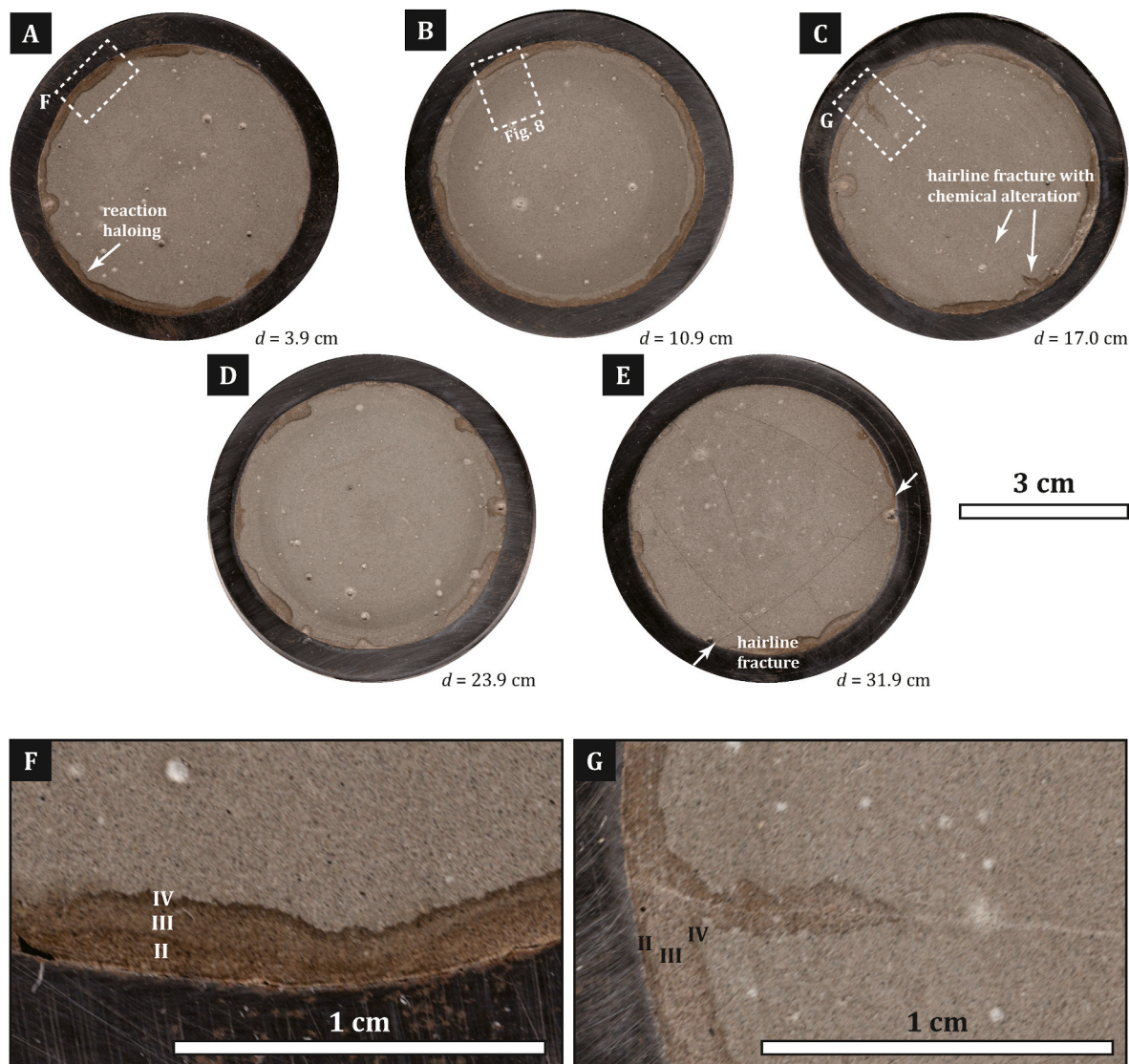
Fig. 7. Reflected light images of successive sections through the cemented steel pipe of Sample B. Distance from the inlet face of the cement plug, *d* [mm], is specified for each cross-section. Azimuthal orientation may vary between sections. Roman numerals indicate reaction zonation (see main text), white arrows in subfigure 7e indicate trace of fracture without signs of chemical alteration.

3.2.2. Cement alteration and zonation

All samples showed similar chemical alteration, with distinct discoloration patterns in the cement matrix bordering the microannuli and larger fractures. Optically, the reaction pattern consisted of a succession of three, sometimes four alteration zones (denoted Zones II-V in Figs. 7–8, S6-S10). Very pale orange to tan or brown colored bands and haloes developed locally at surfaces directly exposed to defects (referred to as Zone II for consistency with previous work; e.g., Wolterbeek et al., 2016b). The width of Zone II varied substantially, reaching up to 1 mm in places while seemingly absent elsewhere, even along one single defect structure. Where present, Zone II was followed by a light brownish to greyish band of similar width (Zone III). In some samples, Zones II and III were difficult to distinguish and appeared to gradate into one another or form a series of multiple minor fronts (Fig. S6). Along cracks in Sample A, Zone II and III could not be discerned optically, with a light grey region bordering directly on white lines marking (possibly precipitation clogged) hairline fractures. Next in the succession, usually a relatively sharp and well-defined dark grey to reddish brown reaction band was observed (Zone IV). This darker front appeared relatively dense. In at least one sample, Zone IV was followed by a lighter grey band, tentatively designated Zone V (Fig. S8).

The combined width of discoloration in the cement varied very noticeably. For example, the thickness of alteration zones adjacent to microannuli measured well below 1 mm along most the circumference of the steel-cement interface, except for a few apparent channels around which much wider, roughly concentric alteration haloes developed (e. g., Fig. 7d; see also white arrows in Figs. S6b and S7a). Besides chemical zonation, some sections showed very regular concentric patterns in the cement matrix, visible as a lighter shade rim adjacent to the steel pipe (Figs. S7d and S7e). These features are artefacts from the rotating lave used to even out the sawcuts prior to grinding and polishing, which proved difficult to grind away completely. Throughout the cement, some of the pores contained white precipitates while other pores remained open (e.g., Fig. S8c).

For Sample B, Fig. 8 shows µXRF maps with relative element abundance for Ca, Si, Al, S, Sr, Mg, Na, Cl and K, where lighter shades correspond to higher concentrations (see also Figs. S9 and S10 for µXRF maps of Samples A and D). The µXRF maps illustrate the chemically zoned nature of the cement surrounding defects. Zone II was characterized by lower Ca and Si relative concentrations. Compared to Zone II, Zone III showed slightly higher Ca, at levels comparable with unaltered cement. Zone IV was low in Ca while relatively enriched in Si. The
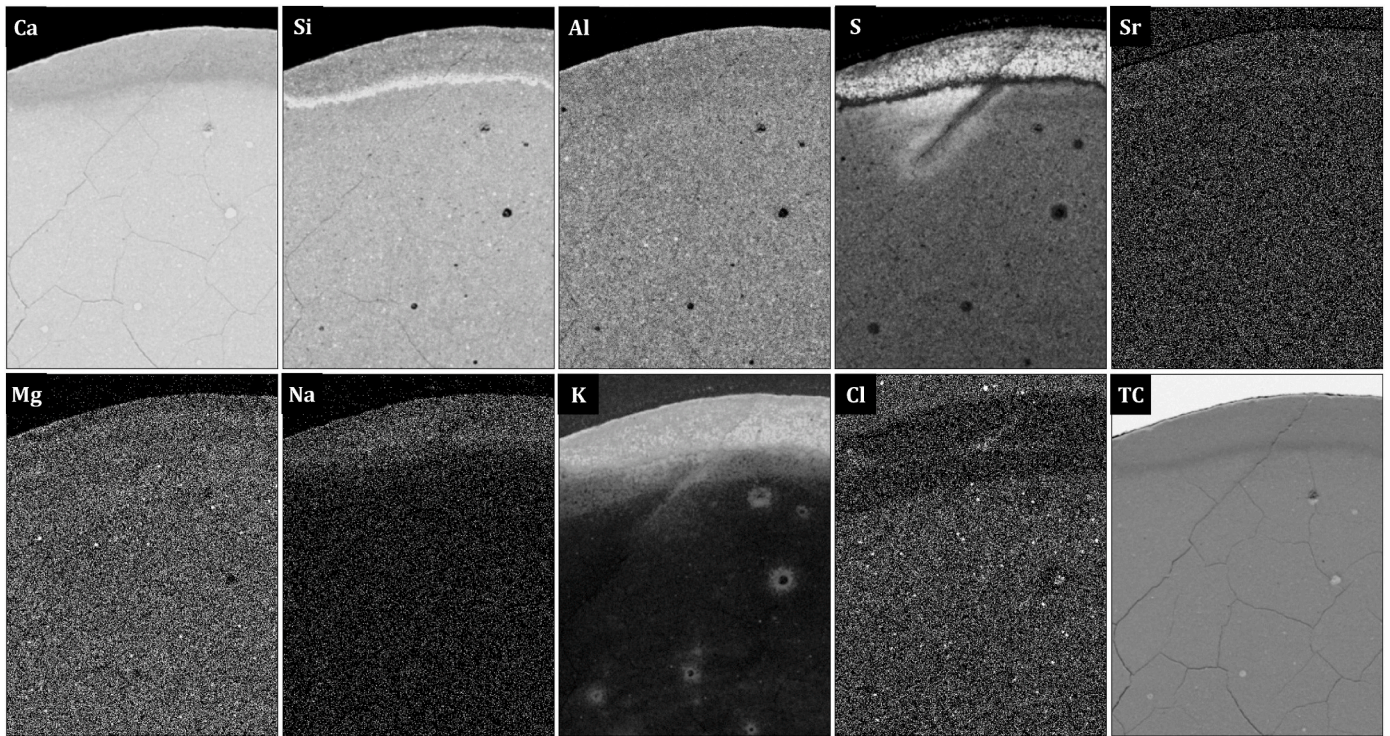
Fig. 8. Micro-X-ray fluorescence maps for Ca, Si, Al, S, Sr, Mg, Na, Cl and K, showing an area containing fractures in the middle of the second cross-section through Sample B (mapped region indicated on Fig. 7b). Grey scale is defined per element and qualitatively shows relative abundance, with brighter illumination corresponding to higher concentrations. The TC map shows total count results for the mapped region.

alteration zones further showed increased K and Sr relative abundances, while S was mostly lowered but elevated in other places. Mg patterns tended to follow Ca, while Sr was relatively enriched around defects. Elevated Ca concentrations along the casing-cement interface (Fig. 8 and S10) indicate some carbonate precipitation occurred in the microannuli here. Interestingly, no elevated Ca was found in the seemingly clogged fractures of Sample A (Figs. S6 and S9).

Chemical zonation appeared to be relatively uniform in successive sections through the plugs, i.e., little variation was observed along the overall direction of flow. Qualitatively, the alteration zone thickness diminished slightly with increasing distance from the inlet face of the cement plug, but thickness variations seen within single sections were much larger by comparison, with alteration effects being confined to haloes around specific conduits for flow along the circumference of the steel-cement interface (Fig. 7d–S6b and S7a). No clear trends with distance from the CO_2 source could be discerned, except for at the inlet and outlet faces of the cement plugs, where the external surfaces were exposed directly to CO_2 (Fig. S11). While the US face showed no obvious signs of extensive cement chemical alteration, the DS ends generally displayed a 0.1–0.5 mm thick alteration layer of yellow-brownish color with white precipitates. The relatively extensive alteration at the tops of the plugs is somewhat remarkable, considering it occurs in a "reversed" position compared to observations in reactive flow-through experiments using CO_2-rich aqueous fluids. Note the plug tops were submerged in liquid water during humid CO_2 flow, which probably contributed to this alteration.

3.3. Estimation of hydraulic aperture, defect volume, and residence time

To compare the experiments with numerical models, the sample defects must be characterized in terms of their void volume, V_a [m^3], and aperture, w [m]. These properties were estimated from microstructural and permeability data. For single-phase flow in a circumferential microannulus, the hydraulic aperture can be inverted from (Bird

et al., 2002; Wolterbeek et al., 2016b):

$$\kappa_{app} = \frac{1}{8r_s^2}\left(r_s^4 - (r_s - w_H)^4 + \frac{w_H^2(2r_s - w_H)^2}{\ln(1 - w_H/r_s)}\right) \tag{2}$$

Here, r_s [m] is the pipe inner radius and w_H [m] is the microannulus aperture. The associated void volume becomes V_{aH} [m^3] $= \pi(r_s^2 - (r_s - w_H)^2)$. Note this method underestimates the aperture and void volume because: i) data were obtained under multiphase flow conditions, which yields effective gas permeability rather than absolute permeability, and ii) the physical defects were non-uniform and hydraulic estimates are sensitive to local restrictions (Wolterbeek and Raoof, 2018). Microstructure-based aperture estimates, w_M [m], were obtained from measurements on sample cross-sections, with $V_{aM} = \pi(r_s^2 - (r_s - w_M)^2)$.

The residence time of CO_2-rich fluid, τ [s], was estimated using two methods. The first involved calculation of the "turnover time" (Wolterbeek et al., 2019), using the flowrate at the start of CO_2 injection:

$$\tau_Q = \frac{2V_a}{(Q_{in} + Q_{out})_{\theta=0}} \tag{3}$$

Here, τ_Q [s] is the flowrate-based residence time, with τ_{QH} and τ_{QM} based on V_{aH} and V_{aM}, respectively (note θ [s] is defined in Equation S1c). As our experiments involved multiphase flow, assessing how accurate such estimates are is challenging. Actual residence times may have been shorter if CO_2-flow occurred via a small subvolume of otherwise waterlogged defects. Conversely, the physical defect volume will have included contributions from local widenings such as macropores (so $V_a \leq V_{defect}$), which could increase actual residence times.

Another estimate for CO_2 residence time was obtained from fluid density data, defining τ_D [s] as the time delay between the moments at which the influent and effluent fluid density increased above N_2 reference values. Note τ_D overvalues the actual residence time, as this estimate also includes the volume of tubing in between the Coriolis meters.

The various residence time estimates are summarized in Table 1.

4. Discussion

Our reactive flow-through experiments on cement-plugged pipes containing microannuli of 2–20 μm wide showed that, after establishment of stable humid N_2 flow, subsequent introduction of humid CO_2 caused decreases in effective permeability of several orders of magnitude. This reduction occurred in two steps: an initial drop of roughly one order of magnitude in the initial 30–60 min after introduction of CO_2, followed by a more gradual slowdown of flow, with κ_{eff} decreasing slowly but steadily for several days. In at least three of the four samples, κ_{eff} ultimately reached down to typical cement matrix permeability values, suggesting effective self-sealing. Microstructural analysis showed all samples contained microannuli along their steel-cement interfaces, complemented by tensile fractures in Sample A and hairline cracks in Samples B and C. Chemical reaction with CO_2 produced alteration zones in the cement that ran alongside or haloed around specific sectors of the defects. Evidence for mineral precipitation-induced clogging is scarce, but some parts of the cracks and microannuli appear carbonate cemented. In the following, we will analyze our results and attempt to explain the main trends seen and discuss differences with earlier work. Subsequently, we evaluate the impact on 'critical residence time'-based model predictions of cement self-sealing and will consider implications for seepage risk.

4.1. Possible permeability reduction mechanisms

4.1.1. Dissolution-precipitation reaction effects

The samples showed relatively little change under humid N_2 flow, except increasing κ_{eff} with progressive displacement of initial water from the cement plug microannuli, especially upon variation of the imposed ΔP in Sample C (Fig. 5 and S4). Nevertheless, observations during N_2 flow suggest little chemical reaction occurred in this stage, consistent with previous work on cement plus water (Wolterbeek et al., 2016b). The reductions in κ_{eff} seen after introduction of CO_2, combined with evidence for alteration along defects, are also consistent with earlier observations of CO_2-induced reactive transport and self-sealing (Carey et al., 2010; Wolterbeek et al., 2016b, 2019). Given these similarities, let us first consider whether aqueous phase dissolution-precipitation reactions can account for the strong κ_{eff} decreases observed here. We evaluate this hypothesis in the context of earlier work.

As summarized in the Introduction, it is well-established that Portland cement reacts chemically with CO_2-rich brines (Carey, 2013). Our experiments show similar cement alteration, with Zones II-IV corresponding roughly to Zones Z2-Z4. Yet, our Zone III is more diffuse than typical for Zone Z3, which usually forms a sharp carbonation front. The lighter colored Zone V in Sample D coincides with regions of increased K on the μXRF maps, particularly where these extend beyond zones of changed Ca and Si content. To our knowledge, elevated K has not been reported for CO_2-cement alteration before. This observation led us to reprocess some earlier μXRF measurements for samples of Wolterbeek et al. (2016b, 2019), which revealed the K-zonation also developed during exposure to CO_2-rich water. Redistribution of K thus seems not unique to humid CO_2 alteration but rather a general carbonation feature. Furthermore, a porous Zone Z1 has not developed in the present samples. In fact, the overall extent of alteration and dissolution upon exposure to humid CO_2 flow seems to be much more limited compared to earlier work using CO_2-rich aqueous fluids (Luquot et al., 2013; Wolterbeek et al., 2016b). This milder reaction can be beneficial, as excessive leaching and degradation are much less likely when there is no water into which the cement phases and carbonates can dissolve and be advectively removed. However, the milder reaction may also impair self-sealing mechanisms, e.g., if insufficient Ca gets liberated to facilitate carbonate precipitation (Wolterbeek and Hangx, 2021). In batch

reaction experiments, Wolterbeek et al. (2013) noted that acicular aragonite formed in the interfacial debonding defects of steel-cement samples exposed to carbonated brine but was not observed in samples suspended above the brine, i.e., subjected to humid CO_2 conditions. Likely, carbonates such as aragonite only precipitate effectively from aqueous solution, hampering mineral clogging of defects that are largely CO_2-filled. This effect of low water-saturation was also considered by Iyer et al. (2018), inferring reduced self-sealing potential using their numerical model.

While we do observe the telltale combination of permeability reduction and cement carbonation in our experiments, direct indications for defect clogging are scarce. The most compelling evidence is provided by the μXRF maps, which locally show elevated Ca concentrations along casing interfaces, suggesting calcium carbonates formed in the microannuli (Fig. 8 and S10). Yet, microstructural observations provided only limited signs of mineralization in microannuli or cracks (Figs. S6 and S9). Part of the challenge here is the small size of the microannuli under study, since steel smearing during polishing could easily obscure fine but important details along the casing interface. Nevertheless, in lieu of indisputable microstructural evidence for carbonate precipitation and defect clogging in the humid CO_2 flow-through experiments, other mechanisms that may have contributed to the observed permeability decrease should be considered.

4.1.2. Capillary effects

Unlike earlier studies, our reactive transport experiments were conducted under definite multiphase flow conditions. During the reference measurements, the two fluid phases involved were liquid water and humid N_2. The latter was replaced by humid [N_2+CO_2] in the reactive stage. When two poorly miscible fluids are present in a network of narrow conduits, interactions of forces between these fluids and the solid conduit walls give rise to capillary pressures (Bikkina and Shaik, 2018). Depending on whether a fluid is wetting or non-wetting, capillary effects can enhance or inhibit flow, e.g., impede entry into conduits of a specific size. For a planar defect, the capillary pressure in a two-fluid system can be described using the Young-Laplace equation (Brown, 2000):

$$P_{cap} = \frac{2\gamma \cos \theta_w}{w} \qquad (4)$$

Here, P_{cap} [Pa] is the capillary pressure, γ [N m^{-1}] is the interfacial tension between the two fluids, θ_w [-] is the contact angle of the wetting fluid, and w [m] is the defect aperture. Entry into porosity can be described similarly, using pore throat radius instead of w.

The plugs in our tests were initially close to water saturated. Portland cement is highly hygroscopic and water-wetting, so the humid N_2 likely would have had to overcome capillary entry pressures to displace the water and permeate into defects or the cement porosity. Evidence for such capillary action is provided by reference measurements on Sample C, where temporarily increasing ΔP probably enabled drainage of narrower defects or parts of the cement porosity, which would result in additional pathways for N_2 flow and hence could explain the irreversible increase in κ_{eff} observed. If the interfacial properties of N_2–H_2O and CO_2–H_2O systems are sufficiently different, capillary effects may similarly affect κ_{eff} upon switching from N_2 to CO_2 flow. For this to explain the rapid permeability drops observed, however, a marked increase in capillary pressure would be required, which is unlikely as we will explain below.

Relevant data on γ between water and [N_2+CO_2] phases is provided by Yan et al. (2001) and Wesch et al. (1997). Representative θ_w data for wet cement are more difficult to obtain. Factors like surface roughness, heterogeneities and contaminations also cause much scatter in wetting data for mineral surfaces in general (Bikkina and Shaik, 2018). To gauge the impact of θ_w, let us first consider complete wetting ($\theta_w = 0°$). Under this assumption, the P_{cap} to enter waterlogged conduits is *lower* for CO_2 than for N_2, due to the lower γ of CO_2–H_2O ($\sim$44 mN m^{-1}) compared to

N_2–H_2O (~63 mN m^{-1}) at 60 °C, 7.8 MPa (Fig. 9).

Let us now consider potential changes in the wetting angle upon switching from N_2 to CO_2. Any increases in θ_w only reduce P_{cap} further. A significant lowering of θ_w would be required for P_{cap} to increase. For example, postulating a reduction from 45° during N_2 flow to 0° during CO_2 flow brings the P_{cap} for CO_2 on par with N_2 only. Though not impossible, given the above it seems unlikely that capillary effects alone would explain the permeability drops. Numerical simulations of gas invasion in our cement plugs using MoReS (Regtien et al., 1995) corroborate this mechanism does not lead to water expulsion into the microannuli. Significant relative permeability changes due to capillary effects are hence considered unlikely.

4.1.3. Changes in multiphase flow pattern

Aside from capillary action, two-phase flow provides other opportunities for relative permeability effects. Multiphase transport can manifest in a wide range of different flow patterns (Brennen, 2005; Dziubinski et al., 2004; Weisman, 1983), including bubbly flow, slug or intermittent flow, annular flow, rivulet flow, and mist flow. Flow pattern development is governed by many factors, including the conduit dimensions, the material properties of the conduit walls, the properties of the fluid phases involved, and their flow rates (Ali et al., 1993; Brennen, 2005; Helmig, 1997). Theoretically, differences in the properties of N_2 and CO_2 could cause changes in flow pattern upon switching fluids. In Sample D, for example, measured densities suggest the [N_2+CO_2] fluid became oversaturated with water upon imposing larger ΔP, pointing to mist flow-like conditions. Note that influent fluid density also increased, which may indicate water got entrained from the reactor vessel instead.

Unfortunately, flow pattern maps are empirical in nature and usually constructed using air-water system measurements, with limited data available for other fluids (Thome and Cioncolini, 2016). We were unable to find data relevant to our fluids and conditions. Notably, natural gas seepage in small defects is generally believed to occur as continuous gas phase migration, because i) the P_{cap} required for a gas bubble to invade a planar conduit is twice that of a continuous phase into the same conduit, and ii) bubble ascent mechanisms are much slower than reported seepage ascension rates (Brown, 2000). Such arguments likely hold for CO_2 seepage as well. Nevertheless, it cannot be ruled out that changes in flow regime such as increased water holdup contributed to the κ_{eff} decrease observed.

4.1.4. Cement porewater volume change upon CO_2 solvation

Carbon dioxide differs from phases such as nitrogen or natural gas in being much more soluble in aqueous fluids. Partly due to dissociation via Reaction R1, ~40 g of CO_2 per kg H_2O can dissolve at 60 °C and 7–8 MPa

(Diamond and Akinfiev, 2003), versus only ~0.9 g of N_2 or CH_4 (Culberson and McKetta, 1951; Wiebe et al., 1933). As with any solute, when CO_2 dissolves in water this causes changes in the mass, density and volume of the resulting solution phase (so-called volume change of mixing). Under our experimental conditions (60 °C, 7–8 MPa), dissolution of CO_2 into water until saturation ($x_{CO_2} = 0.016$ mol mol^{-1}) involves a mass increase of ~4% (Diamond and Akinfiev, 2003), while the density of the resulting aqueous solution increases only ~1%, assuming a typical apparent molar volume of dissolved CO_2 of 35 cm^3 mol^{-1} (Figure 13 of Hu et al., 2007). Dissolution of CO_2 into water thus produces a net increase in aqueous solution volume of about 3% at 60 °C, 7–8 MPa (Hassanzadeh et al., 2008). In our experiments, this swelling effect will also occur as CO_2 replaces N_2 and begins to dissolve in the cement porewater.

The excess volume of porewater thus created could get expulsed and cause relative permeability effects in the microannuli. Assuming a Fickian diffusion process with an effective diffusion coefficient for CO_2 in the cement of $D_{cem} = 1.8 \bullet 10^{-10}$ m^2 s^{-1} (Patel et al., 2016), the invasion depth into the cement matrix can be approximated as $x_{in} = \sqrt{D_{cem}t}$, where t [s] is exposure time. Considering the 30–60 min periods in which the initial κ_{eff} decreases occurred, x_{in} ranges from 500 to 800 µm. Taking a typical cement porosity of $\varphi = 0.2$ [-] (Nelson and Guillot, 2006) and assuming water flow in the defect can be neglected (note this assumption will have to break down eventually), expulsion of excess porewater volume associated with CO_2-solvation could cause microannular water films to swell by up to ~5 µm in 1 h. Since the defects in our experiments were relatively small (2–20 µm), this constitutes a significant increase in defect water saturation and may hence have effectively decreased relative permeability with respect to CO_2 (Fig. 10).

4.2. Comparison with 'critical residence time'-based models

Numerical modelling of CO_2-cement reactive transport processes has shown that the conditions for sealing vs. non-sealing behaviour seen in experiments using carbonated brine can be characterized in terms of the i) initial defect aperture, w [m], and ii) residence time of the CO_2-rich aqueous fluid, τ [s] (Brunet et al., 2016; Cao et al., 2015; Iyer et al., 2017, 2018). The latter is usually defined as:

$$\tau = \frac{V_{defect}}{Q} \tag{5}$$

Here, V_{defect} [m^3] denotes defect volume and Q [m^3 s^{-1}] is the flowrate (Brunet et al., 2016; Wolterbeek et al., 2019). Qualitatively, the models show that i) narrower defects seal more easily and ii) longer residence times promote sealing. Sufficient time is needed to liberate
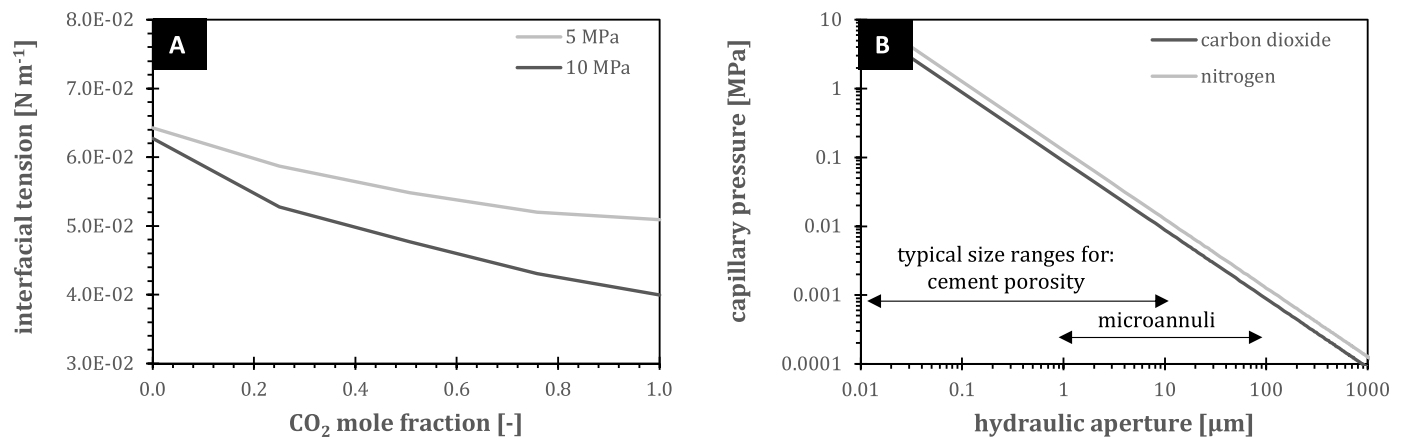
Fig. 9. Plots of a) interfacial tension of [N_2+CO_2] with water as a function of composition at 60 °C, and b) capillary entry pressures for N_2 and CO_2 into water-filled conduits as a function of conduit aperture, at 60 °C and 7.8 MPa. Plotted trends are based on data for [N_2+CO_2]–H_2O from Yan et al. (2001) and Wesch et al. (1997), assuming complete water wetting of the cement ($\theta_w = 0°$). Typical size ranges for cement porosity and casing-cement microannuli are indicated.
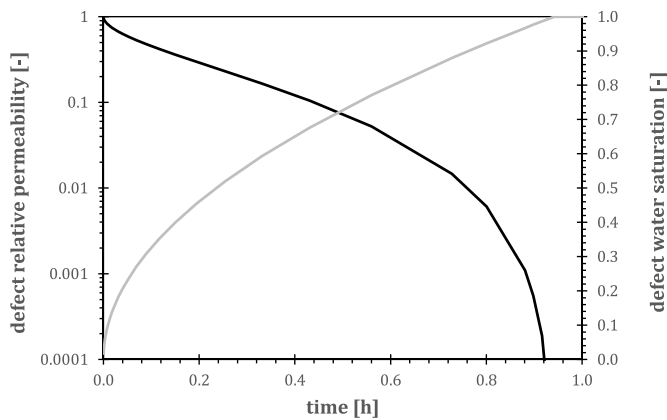
Fig. 10. Defect water saturation (grey) and resulting gas permeability reduction (black) with time due to CO_2-solubility induced cement porewater expulsion. Calculations assume formation of a stagnant water film and corresponding reduction of the effective hydraulic aperture for flow in the defect. Note the calculations predict about 1 order decrease in relative permeability in 30 min after switching to CO_2 flow.

enough Ca and produce pH conditions for carbonate precipitation via Reaction R4, whereas short residence times allow Reaction R2-R3 to proceed without accumulating the Ca concentrations required for carbonate precipitation. Typically, this reactive transport behaviour is captured in terms of a 'critical residence time', τ_{crit} [s]. Self-sealing can be expected if the duration fluid spends in contact with the cement exceeds this threshold value.

Fig. 11a shows model predictions by Brunet et al. (2016) and Iyer et al. (2017), together with data from earlier experiments involving exposure of cement defects to flowing CO_2-rich aqueous fluids. Lab samples which displayed a persisting reduction in permeability down to impermeable values (plotted in green) are located inside the self-sealing region as defined by Brunet et al. (2016), while experiments that showed no tendency for permeability decrease (data in orange) largely plot below the critical boundary of Iyer et al. (2017). Samples denoted as 'limited sealing' (data in grey) showed some degree of permeability reduction (typically 1-2 orders) but did not attain an "impermeable condition" on the timescale of the experiments, leaving their ultimate fate undetermined (note most limited sealing samples showed a stable permeability following the initial drop, but a few cases displayed very gradual increases with time).

While points at issue remain (Guthrie et al., 2018; Wolterbeek et al., 2019), the 'critical residence time' concept seems generally effective in predicting sealing under flow of CO_2-rich aqueous fluids (Fig. 11a). Given this success with carbonated brine, let us consider whether the concept can also explain our results under humid CO_2 flow. With τ_{crit} ranging from 30 to 330 s for defects of 2–20 μm, it should be noted that estimates for τ in our experiments showed significant spread, varying from seconds to hours (Table 1). If τ_Q is taken as reference, i.e., using flow-based estimates similar to those used to construct Fig. 11a (cf. Equations (3) and (5)), then subcritical durations of 2–21 s are obtained. This suggests precipitation alone would produce limited sealing only (Fig. 11b). Yet, our samples showed κ_{eff} reductions down to cement matrix permeabilities (below $\sim 10^{-17}$ m^2), implying persistent self-sealing. We postulate two-phase fluid interactions produced an initial slowdown of flow, which extended residence times and thereby enabled carbonate precipitation and sealing. The τ_Q-values then represent inflow of CO_2 only, with N_2 still being the outflowing medium. By the time CO_2 was registered downstream of the cement plugs, the flowrates were demonstrably much lower already, as shown by the time delay between density changes in the influent and effluent fluid, yielding τ_D of 1–12 h (Table 1). For these extended residence times, our plug samples plot well within the sealing regime of Brunet et al. (2016),
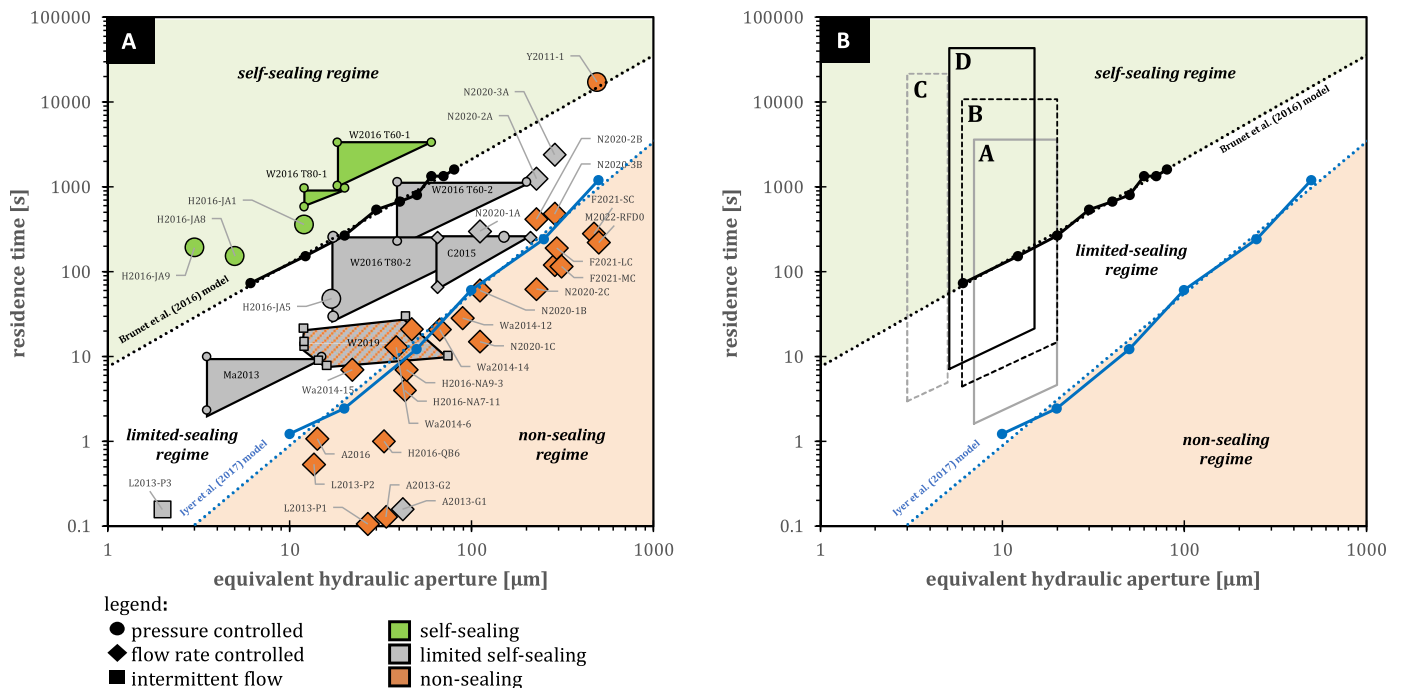

Fig. 11. Self-sealing and non-sealing behavior of CO_2 reactive transport in wellbore defects as predicted by the numerical models of Brunet et al. (2016) and Iyer et al. (2017), plotted in residence time versus hydraulic aperture space, with a) experimental data for flow of CO_2-rich aqueous fluids. Circles, diamonds, and squares represent lab tests conducted under pressure controlled, flowrate controlled, and intermittent flow conditions, respectively. Specific labels include the following codes per study, appended by experiment names as in the original publications: A2016, A2013 = Abdoulghafour et al. (2016, 2013); C2015 = Cao et al. (2015); F2021 = Fernandez-Rojo et al. (2021); H2016 = Huerta et al. (2016); L2013 = Luquot et al. (2013); Ma2013 = Mason et al. (2013); M2022 = Miao et al. (2022); N2020 = Nguyen et al. (2020); Wa2014 = Walsh et al. (2014); W2019, W2016 = Wolterbeek et al. (2019, 2016b); Y2011 = Yalcinkaya et al. (2011). Figure b) shows defect aperture and humid CO_2 residence time estimates for the present experiments, denoted A-D (Table 1). See main text for discussion.

consistent with the late stage permeability reductions observed.

Under multiphase flow conditions, it should be noted that the different fluids involved may have diverging residence times. Liquid holdup will likely cause the τ of the aqueous fluid to exceed that of the CO_2 phase. Since dissolution-precipitation reactions require an aqueous fluid medium to occur effectively, sealing vs. non-sealing behaviour will likely depend predominantly on the aqueous phase residence time, rather than on the residence time of the CO_2-dominated phase (see also Iyer et al., 2018). Unfortunately, this parameter was found challenging to constrain confidently in our experiments.

4.3. Implications for self-sealing potential along cemented wellbores

The present experiments demonstrate that, similar to flow of CO_2-rich aqueous fluids, reactive transport of humid supercritical CO_2 can lead to progressive self-sealing of seepage along cemented wellbores, at least in small defects with apertures of 2–20 μm. It seems 'critical residence time'-based criteria for delineating sealing and non-sealing reactive transport regimes (Brunet et al., 2016; Cao et al., 2015; Iyer et al., 2017) can be applied to humid CO_2 seepage to within current experimental error. In general, the boundary between sealing and non-sealing behaviour is not sharp (e.g., limited sealing regime in Fig. 11).

Considering differences between seepage of CO_2-rich versus water-rich fluids, the reduced precipitation potential at lower water saturations inferred by Iyer et al. (2018) warrants further study. Nevertheless, this reduction seems to be partially off-set by other multiphase flow effects, notably CO_2-solvation induced swelling of the cement pore-water. Unfortunately, sample preparation methods employed in the current study limited the maximum defect size to 20 μm. More research is needed to assess whether porewater swelling also contributes to sealing in larger-scale defects, noting the phenomenon probably becomes less impactful with increasing aperture size. On the other hand, our humid CO_2 flow experiments did show markedly less severe cement alteration compared to typical CO_2-rich brine flow experiments. Specifically, the formation of an extensively reacted, enhanced porosity region in the cement (Zone Z1 as discussed in Section 4.1.1) was not observed in any of the present samples, despite injection of large volumes of CO_2-rich fluid. Since ionic transport requires an aqueous fluid, degradation (i.e., loss of cement functionality) due to advective removal of leached species from the cement also becomes considerably less likely with decreasing water saturation. In this context, it is interesting to note Zone Z1 seems absent in CO_2-exposed cements recovered in well field studies (Carey et al., 2007; Crow et al., 2010; Duguid et al., 2014). When using self-sealing criteria like those proposed by Brunet et al. (2016) or Iyer et al. (2017) to analyze CCS well integrity, it is important to calculate the expected residence time on basis of the aqueous fluid phase and not the humid CO_2 phase (i.e., account for liquid holdup), because the brine flowrate will determine the balance between advective dissolution-removal and precipitation-clogging reactions.

5. Conclusions

This study investigated the impact of humid CO_2 seepage on the transport properties of defects in wellbore cement-casing systems. Four reactive flow experiments were conducted on 30 cm-long cement plugged steel pipes containing 2–20 μm wide microannuli. The experiments were performed at 60 °C and 7 MPa, by applying pressure differences of 0.2–1.6 MPa, while measuring resultant flows. Following initial reference flow experiments using humid N_2, the introduction and ingress of humid CO_2 were monitored via inline fluid density measurements. After completion of the reactive flow experiments, the samples were subjected to microstructural study. The main findings are as follows:

1. The cemented pipes were first subjected to humid N_2 flow until a stable effective permeability was attained, resulting in initial values of $2.5 \cdot 10^{-16}$ m^2 to $2.2 \cdot 10^{-15}$ m^2. This N_2 stage also preconditioned the multiphase flow pattern in the cement plugs, simulating natural gas seepage and displacement of water from defects prior to arrival of CO_2 at a legacy well.
2. Switching from N_2 to CO_2 flow produced a rapid decrease in effective permeability (about one order of magnitude in 30–60 min), followed by more gradual self-stoppage of flow. All four samples attained effective permeabilities on par with typical values for intact, good quality cement well isolations, implying effective sealing of the defects.
3. Microstructural analysis revealed moderate cement alteration. The reaction zonation developed due to humid CO_2 flow agrees broadly with that documented in earlier studies involving exposure to CO_2-rich aqueous fluids. Yet, extensively leached zones of enhanced porosity ("Z1") were notably not observed in our samples exposed to humid CO_2. Evidence for carbonate precipitation in open defects was also limited compared to earlier studies using CO_2-rich aqueous fluids.
4. Given the above, mechanisms other than carbonate precipitation have been considered as possible causes of the initial permeability drops observed. Multiphase flow phenomena, specifically relative permeability effects due to CO_2 solvation-induced swelling and expulsion of the cement porewater, are identified as viable explanations for the initial decrease in flowrate. Analysis in the context of 'critical residence time'-based models shows that an initial drop in flowrate caused by multiphase flow phenomena could have been sufficient to jumpstart carbonate precipitation and thereby the progressive self-sealing observed in the later stages of the experiments.
5. Our results show that 'critical residence time'-based criteria for delineating sealing versus non-sealing reactive transport can also be applied to seepage of humid CO_2, at least for microannuli of 2–20 μm wide. Further research is needed to assess the impact of humid CO_2 flow on larger defects, as the here identified porewater-swelling effect is likely most impactful in narrow apertures.

CRediT authorship contribution statement

T.K.T. Wolterbeek: Conceptualization, Formal analysis, Investigation, Methodology, Visualization, Writing – original draft, Writing – review & editing. **J.R. Snippe:** Formal analysis, Visualization, Writing – review & editing. **S.J.T. Hangx:** Visualization, Writing – review & editing.

Declaration of competing interest

The authors declare that they have no known competing financial interests or personal relationships that could have appeared to influence the work reported in this paper.

Data availability

Data will be made available on request.

Appendix A. Supplementary data

Supplementary data to this article can be found online at https://doi.org/10.1016/j.geoen.2024.212728.

List of symbols

Symbol	Description
A	Internal cross-sectional area cemented pipe [m^2]
D_{cem}	Effective diffusion coefficient for CO_2 in wet cement [$m^2\ s^{-1}$]
φ	Porosity [-]
γ	Interfacial tension between two fluids [$N\ m^{-1}$]
κ_{eff}	Effective permeability of sample [m^2]
L	Length of the cement plug [m]
M	Molar mass of seepage fluid [$kg\ mol^{-1}$]
$\dot{m}_{DS}$	Downstream (effluent) mass flowrate [$kg\ s^{-1}$]
$\dot{m}_{US}$	Upstream (influent) mass flowrate [$kg\ s^{-1}$]
$\overline{\mu}$	Mean fluid dynamic viscosity [Pa s]
P_{cap}	Capillary entry pressure [Pa]
P_{DS}	Fluid pressure in downstream pump [Pa]
P_{US}	Fluid pressure in upstream pump [Pa]
P_{in}	Fluid pressure at inlet of sample [Pa]
P_{out}	Fluid pressure at outlet of sample [Pa]
ΔP	Differential pressure over cement plug [Pa]
Q	Volumetric fluid flowrate [$m^3\ s^{-1}$]
Q_{DS}	Flowrate measured in downstream pump [$m^3\ s^{-1}$]
Q_{US}	Flowrate measured in upstream pump [$m^3\ s^{-1}$]
Q_{in}	Volume flowrate going into the sample [$m^3\ s^{-1}$]
Q_{out}	Volume flowrate coming out of the sample [$m^3\ s^{-1}$]
R	Gas constant [$J\ K^{-1}\ mol^{-1}$]
r_s	Factory inner radius of the steel casing pipe used to prepare samples [m]
ρ_{DS}	Density of the effluent (downstream) fluid [$kg\ m^{-3}$]
ρ_{US}	Density of the influent (upstream) fluid [$kg\ m^{-3}$]
T	Temperature [°C]
T_{in}	Fluid temperature at inlet of sample [°C]
T_{oven}	Temperature of oven housing sample [°C]
τ	Residence time of CO_2-rich fluid in the cemented pipe sample [s]
τ_{crit}	Critical residence time for defect self-sealing [s]
τ_D	Humid CO_2 residence time (estimate based on ρ_{US} and ρ_{DS}) [s]
τ_{QH}	Humid CO_2 residence time (estimate based on w_H) [s]
τ_{QM}	Humid CO_2 residence time (estimate based on w_M) [s]
θ	Mean time of measurement interval; see Equation S1c [s]
θ_w	Contact angle of wetting fluid [-]
V_{DS}	Volume downstream pump [m^3]
V_{US}	Volume upstream pump [m^3]
V_{aH}	Defect void volume (estimate based on w_H) [m^3]
V_{aM}	Defect void volume (estimate based on w_M) [m^3]
V_{defect}	True defect void volume [m^3]
w	Defect aperture [m]
w_H	Defect hydraulic aperture (estimate based on flow data) [m]
w_M	Defect aperture (estimate based on microstructure data) [m]
x_{CO_2}	Mole fraction of dissolved CO_2 in aqueous fluid [$mol\ mol^{-1}$]
x_{in}	Diffusive invasion depth of CO_2 into cement matrix [m]
$\overline{z}$	Mean compressibility factor [-]

References

Abdoulghafour, H., Gouze, P., Luquot, L., Leprovost, R., 2016. Characterization and modeling of the alteration of fractured class-G Portland cement during flow of CO_2-rich brine. Int. J. Greenh. Gas Control 48, 155–170.

Abdoulghafour, H., Luquot, L., Gouze, P., 2013. Characterization of the mechanisms controlling the permeability changes of fractured cements flowed through by CO_2-rich brine. Environ. Sci. Technol. 47, 10332–10338.

Ajayi, T., Gupta, I., 2019. A review of reactive transport modeling in wellbore integrity problems. J. Petrol. Sci. Eng. 175, 785–803.

Ali, M.I., Sadatomi, M., Kawaji, M., 1993. Adiabatic two-phase flow in narrow channels between two flat plates. Can. J. Chem. Eng. 71, 657–666.

API RP 10B-2, 2013. Recommended Practice for Testing Well Cements. American Petroleum Institute.

Barclay, I., Pellenbarg, J., Tettero, F., Pfeiffer, J., Slater, H., Staal, T., Stiles, D., Tilling, G., Whitney, C., 2001. The beginning of the end: a review of abandonment and decommissioning practices. Oilfield Rev. 13, 28–41.

Belfroid, S., Koenen, M., Kreft, E., Huijskes, T., Neele, F., 2021. CCS at depleted gas fields in North Sea: network analysis. In: Proceedings of the 15th Greenhouse Gas Control Technologies Conference, pp. 15–18.

Beltrán-Jiménez, K., Skadsem, H.J., Sunde, J.K., Gardner, D., Wolterbeek, T.K., Cornelissen, E.K., Keultjes, W.J.G., 2022. Restoration of annular zonal isolation using localized casing expansion (LCE) technology: Treatment of near-horizontal test sections containing a free-water channel. J. Petrol. Sci. Eng. 208, 109792.

Bikkina, P., Shaik, I., 2018. Interfacial tension and contact angle data relevant to carbon sequestration. In: Carbon Capture. utilization and sequestration, pp. 163–186.

Bird, R.B., Stewart, W.E., Lightfoot, E.N., 2002. Transport Phenomena, 2nd edition. John Wiley & Sons, Inc, New York, NY, USA.

Brennen, C.E., 2005. Fundamentals of Multiphase Flows. Cambridge University Press.

Brown, A., 2000. Evaluation of possible gas microseepage mechanisms. AAPG (Am. Assoc. Pet. Geol.) Bull. 84, 1775–1789.

Brunet, J.-P.L., Li, L., Karpyn, Z.T., Huerta, N.J., 2016. Fracture opening or self-sealing: critical residence time as a unifying parameter for cement–CO_2–brine interactions. Int. J. Greenh. Gas Control 47, 25–37.

Brunet, J.-P.L., Li, L., Karpyn, Z.T., Kutchko, B.G., Strazisar, B., Bromhal, G., 2013. Dynamic evolution of cement composition and transport properties under conditions relevant to geological carbon sequestration. Energy Fuels 27, 4208–4220.

Cao, P., Karpyn, Z.T., Li, L., 2015. Self-healing of cement fractures under dynamic flow of CO_2-rich brine. Water Resour. Res. 51, 4684–4701.

Carey, J.W., 2013. Geochemistry of wellbore integrity in CO_2 sequestration: Portland cement-steel-brine-CO_2 interactions. Rev. Mineral. Geochem. 77, 505–539.

Carey, J.W., Svec, R., Grigg, R., Zhang, J., Crow, W., 2010. Experimental investigation of wellbore integrity and CO_2–brine flow along the casing–cement microannulus. Int. J. Greenh. Gas Control 4, 272–282.

Carey, J.W., Wigand, M., Chipera, S.J., Wolde Gabriel, G., Pawar, R., Lichtner, P.C., Wehner, S.C., Raines, M.A., Guthrie, G.D., 2007. Analysis and performance of oil well cement with 30 years of CO_2 exposure from the SACROC Unit, West Texas, USA. Int. J. Greenh. Gas Control 1, 75–85.

Choi, Y.-S., Young, D., Nešić, S., Gray, L.G.S., 2013. Wellbore integrity and corrosion of carbon steel in CO_2 geologic storage environments: a literature review. Int. J. Greenh. Gas Control 16, S70–S77.

Crow, W., Carey, J.W., Gasda, S., Williams, D.B., Celia, M.l., 2010. Wellbore integrity analysis of a natural CO_2 producer. Int. J. Greenh. Gas Control 4, 186–197.

Culberson, O.L., McKetta, J.J., 1951. Phase equilibria in hydrocarbon-water systems III - the solubility of methane in water at pressures to 10,000 psia. J. Petrol. Technol. 3, 223–226.

Diamond, L.W., Akinfiev, N.N., 2003. Solubility of CO_2 in water from −1.5 to 100 °C and from 0.1 to 100 MPa: evaluation of literature data and thermodynamic modelling. Fluid Phase Equil. 208, 265–290.

Dou, H., Dong, X., Duan, Z., Ma, Y., Gao, D., 2020. Cement integrity loss due to interfacial debonding and radial cracking during CO_2 injection. Energies 13, 4589.

Duguid, A., 2009. An estimate of the time to degrade the cement sheath in a well exposed to carbonated brine. Energy Proc. 1, 3181–3188.

Duguid, A., Carey, J.W., Butsch, R., 2014. Well integrity assessment of a 68 year old well at a CO_2 injection project. Energy Proc. 63, 5691–5706.

Dusseault, M.B., Gray, M.N., Nawrocki, P.A., 2000. Why oilwells leak: cement behavior and long-term consequences. In: SPE International Oil and Gas Conference and Exhibition in China. OnePetro, Beijing, China. SPE-64733-MS.

Dusseault, M.B., Jackson, R., 2014. Seepage pathway assessment for natural gas to shallow groundwater during well stimulation, in production, and after abandonment. Environ. Geosci. 21, 107–126.

Dziubinski, M., Fidos, H., Sosno, M., 2004. The flow pattern map of a two-phase non-Newtonian liquid–gas flow in the vertical pipe. Int. J. Multiphas. Flow 30, 551–563.

Emami-Meybodi, H., Hassanzadeh, H., Green, C.P., Ennis-King, J., 2015. Convective dissolution of CO_2 in saline aquifers: Progress in modeling and experiments. Int. J. Greenh. Gas Control 40, 238–266.

Eslami, A., Akbari, S., Taghavi, S.M., 2022. An experimental study of displacement flows in stationary and moving annuli for reverse circulation cementing applications. J. Petrol. Sci. Eng. 213, 110321.

Feng, G., Xu, T., Tian, H., Lu, M., Connell, L.D., Lei, H., Shi, Y., 2017. Three-phase non-isothermal flow behavior of CO_2-brine leakage from wellbores. Int. J. Greenh. Gas Control 64, 183–193.

Fernandez-Rojo, L., Soler, J.M., Dávila, G., Chaparro, M.C., Queralt, I., Cama, J., 2021. Flow and reaction along the interface between hydrated Portland cement and calcareous rocks during CO_2 injection. Laboratory experiments and modeling. International Journal of Greenhouse Gas Control 108, 103331.

Godec, M., Kuuskraa, V., van Leeuwen, T., Melzer, L.S., Wildgust, N., 2011. CO_2 storage in depleted oil fields: the worldwide potential for carbon dioxide enhanced oil recovery. Energy Proc. 4, 2162–2169.

Gorody, A.W., 2012. Factors affecting the variability of stray gas concentration and composition in groundwater. Environ. Geosci. 19, 17–31.

Gu, T., Guo, X., Li, Z., Cheng, X., Fan, X., Korayem, A., Duan, W.H., 2017. Coupled effect of CO_2 attack and tensile stress on well cement under CO2 storage conditions. Construct. Build. Mater. 130, 92–102.

Guthrie, G.D., Pawar, R.J., Carey, J.W., Karra, S., Harp, D.R., Viswanathan, H.S., 2018. The mechanisms, dynamics, and implications of self-sealing and CO_2 resistance in wellbore cements. Int. J. Greenh. Gas Control 75, 162–179.

Hangx, S.J.T., van der Linden, A., Marcelis, F., Liteanu, E., 2016. Defining the brittle failure envelopes of individual reaction zones observed in CO_2-exposed wellbore cement. Environ. Sci. Technol. 50, 1031–1038.

Hassanzadeh, H., Pooladi-Darvish, M., Elsharkawy, A.M., Keith, D.W., Leonenko, Y., 2008. Predicting PVT data for CO_2–brine mixtures for black-oil simulation of CO_2 geological storage. Int. J. Greenh. Gas Control 2, 65–77.

Helmig, R., 1997. Multiphase Flow and Transport Processes in the Subsurface: a Contribution to the Modeling of Hydrosystems. Springer.

Hu, J., Duan, Z., Zhu, C., Chou, I.-M., 2007. PVTx properties of the CO_2–H_2O and CO_2–H_2O–NaCl systems below 647 K: Assessment of experimental data and thermodynamic models. Chem. Geol. 238, 249–267.

Huerta, N.J., Hesse, M.A., Bryant, S.L., Strazisar, B.R., Lopano, C.L., 2013. Experimental evidence for self-limiting reactive flow through a fractured cement core: implications for time-dependent wellbore leakage. Environ. Sci. Technol. 47, 269–275.

Huerta, N.J., Hesse, M.A., Bryant, S.L., Strazisar, B.R., Lopano, C.L., 2016. Reactive transport of CO_2-saturated water in a cement fracture: Application to wellbore leakage during geologic CO_2 storage. Int. J. Greenh. Gas Control 44, 276–289.

Iyer, J., Walsh, S.D.C., Hao, Y., Carroll, S.A., 2017. Incorporating reaction-rate dependence in reaction-front models of wellbore-cement/carbonated-brine systems. Int. J. Greenh. Gas Control 59, 160–171.

Iyer, J., Walsh, S.D.C., Hao, Y., Carroll, S.A., 2018. Assessment of two-phase flow on the chemical alteration and sealing of leakage pathways in cemented wellbores. Int. J. Greenh. Gas Control 69, 72–80.

Jahanbakhsh, A., Liu, Q., Hadi Mosleh, M., Agrawal, H., Farooqui, N.M., Buckman, J., Recasens, M., Maroto-Valer, M., Korre, A., Durucan, S., 2021. An investigation into CO_2–brine–cement–reservoir rock interactions for wellbore integrity in CO_2 geological storage. Energies 14, 5033.

Kjøller, C., Sigalas, L., Frykman, P., Bjørge, R., Torsæter, M., 2016. Cement self-healing as a result of CO_2 leakage. Energy Proc. 86, 342–351.

Kutchko, B.G., Strazisar, B.R., Dzombak, D.A., Lowry, G.V., Thaulow, N., 2007. Degradation of well cement by CO_2 under geologic sequestration conditions. Environ. Sci. Technol. 41, 4787–4792.

Kutchko, B.G., Strazisar, B.R., Hawthorne, S.B., Lopano, C.L., Miller, D.J., Hakala, J.A., Guthrie, G.D., 2011. H_2S–CO_2 reaction with hydrated Class H well cement: acid-gas injection and CO_2 co-sequestration. Int. J. Greenh. Gas Control 5, 880–888.

Kutchko, B.G., Strazisar, B.R., Lowry, G.V., Dzombak, D.A., Thaulow, N., 2008. Rate of CO_2 attack on hydrated class H well cement under geologic sequestration conditions. Environ. Sci. Technol. 42, 6237–6242.

Lecampion, B., Bunger, A., Kear, J., Quesada, D., 2013. Interface debonding driven by fluid injection in a cased and cemented wellbore: modeling and experiments. Int. J. Greenh. Gas Control 18, 208–223.

Lemmon, E.W., McLinden, M.O., Friend, D.G., 2016. Thermodynamic properties of fluid systems. In: Linstrom, P.J., Mallard, W.G. (Eds.), NIST Chemistry Webbook, NIST Standard Reference Dabase Number 69.

Linda, A., Singh, H.P., 2021. Geological carbon capture and storage as a climate-change mitigation technology. Advances in Carbon Capture and Utilization 33–55.

Liteanu, E., Spiers, C.J., 2011. Fracture healing and transport properties of wellbore cement in the presence of supercritical CO_2. Chem. Geol. 281, 195–210.

Luquot, L., Abdoulghafour, H., Gouze, P., 2013. Hydro-dynamically controlled alteration of fractured Portland cements flowed by CO_2-rich brine. Int. J. Greenh. Gas Control 16, 167–179.

Mason, H.E., Du Frane, W.L., Walsh, S.D.C., Dai, Z., Charnvanichborikarn, S., Carroll, S. A., 2013. Chemical and mechanical properties of wellbore cement altered by CO_2-rich brine using a multianalytical approach. Environ. Sci. Technol. 47, 1745–1752.

Mason, H.E., Walsh, S.D.C., DuFrane, W.L., Carroll, S.A., 2014. Determination of diffusion profiles in altered wellbore cement using X-ray computed tomography methods. Environ. Sci. Technol. 48, 7094–7100.

Miao, X., Gan, M., Wang, Y., Zhang, L., Jing, H., 2022. Permeability evolution of defective wellbore cement under geologic carbon sequestration conditions by means of varying-radius pipeline modeling. J. Nat. Gas Sci. Eng. 98, 104393.

Mikunda, T., Brunner, L., Skylogianni, E., Monteiro, J., Rycroft, L., Kemper, J., 2021. Carbon capture and storage and the sustainable development goals. Int. J. Greenh. Gas Control 108, 103318.

Moghadam, A., Castelein, K., ter Heege, J., Orlic, B., 2022. A study on the hydraulic aperture of microannuli at the casing–cement interface using a large-scale laboratory setup. Geomechanics for Energy and the Environment 29, 100269.

Nelson, E.B., Guillot, D., 2006. Well Cementing. Schlumberger Educational Services, Sugar Land, TX.

Nguyen, P., Guthrie, G.D., Carey, J.W., 2020. Experimental validation of self-sealing in wellbore cement fractures exposed to high-pressure, CO_2-saturated solutions. Int. J. Greenh. Gas Control 100, 103112.

OEUK, 2022. Use of Barrier Materials in Well Decommissioning Guidelines, Issue 3. Offshore Energy UK.

Orlic, B., 2009. Some geomechanical aspects of geological CO_2 sequestration. KSCE J. Civ. Eng. 13, 225–232.

Patel, R.A., Phung, Q.T., Seetharam, S.C., Perko, J., Jacques, D., Maes, N., de Schutter, G., Ye, G., van Breugel, K., 2016. Diffusivity of saturated ordinary Portland cement-based materials: a critical review of experimental and analytical modelling approaches. Cement Concr. Res. 90, 52–72.

Procesi, M., Cantucci, B., Buttinelli, M., Armezzani, G., Quattrocchi, F., Boschi, E., 2013. Strategic use of the underground in an energy mix plan: Synergies among CO_2, CH_4 geological storage and geothermal energy. Latium Region case study (Central Italy). Appl. Energy 110, 104–131.

Raoof, A., Nick, H.M., Wolterbeek, T.K.T., Spiers, C.J., 2012. Pore-scale modeling of reactive transport in wellbore cement under CO_2 storage conditions. Int. J. Greenh. Gas Control 11, S67–S77.

Regtien, J.M.M., Por, G.J.A., van Stiphout, M.T., van der Vlugt, F.F., 1995. Interactive Reservoir Simulation. SPE Reservoir Simulation Symposium, San Antonio, Texas, USA.

Rice, A.K., McCray, J.E., Singha, K., 2018. Methane leakage from hydrocarbon wellbores into overlying groundwater: numerical investigation of the multiphase flow processes governing migration. Water Resour. Res. 54, 2959–2975.

Roijmans, R.F.H., Wolterbeek, T.K.T., Cornelissen, E.K., Keultjes, W.J.G., 2023. Evaluating the sealing performance of plug and abandonment cement systems under downhole conditions. SPE J. 1–16.

Schimmel, M., Liu, W., Worrell, E., 2019. Facilitating sustainable geo-resources exploitation: a review of environmental and geological risks of fluid injection into hydrocarbon reservoirs. Earth Sci. Rev. 194, 455–471.

Slowik, V., Schmidt, M., Fritzsch, R., 2008. Capillary pressure in fresh cement-based materials and identification of the air entry value. Cement Concr. Compos. 30, 557–565.

Szulczewski, M.L., MacMinn, C.W., Herzog, H.J., Juanes, R., 2012. Lifetime of carbon capture and storage as a climate-change mitigation technology. Proc. Natl. Acad. Sci. USA 109, 5185–5189.

Taylor, H.F.W., 1997. Cement Chemistry, second ed. Thomas Telford, London, UK.

Thome, J.R., Cioncolini, A., 2016. Unified modeling suite for two-phase flow, convective boiling, and condensation in macro-and microchannels. Heat Tran. Eng. 37, 1148–1157.

van Eijden, J., Cornelissen, E.K., Ruckert, F., Wolterbeek, T.K.T., 2017. Development of Experimental Equipment and Procedures to Evaluate Zonal Isolation and Well Abandonment Materials. SPE/IADC Drilling Conference and Exhibition. OnePetro, The Hague, the Netherlands. SPE-184640-MS.

Walsh, S.D.C., Mason, H.E., Du Frane, W.L., Carroll, S.A., 2014. Experimental calibration of a numerical model describing the alteration of cement/caprock interfaces by carbonated brine. International Journal of Greenhouse Gas Control 22, 176–188.

Weisman, J., 1983. Two-phase Flow Patterns, Handbook of Fluids in Motion. Butterworth Publishers, Woburn, MA, USA, pp. 409–425.

Wesch, A., Dahmen, N., Ebert, K., Schoen, J., 1997. Interfacial tension, drop size, and angle of contact in the H_2O/CO_2 binary system at temperatures of 298-333 K and pressures up to 30 MPa. Chem. Ing. Tech. 69, 942–946.

Wiebe, R., Gaddy, V.L., Heins, C., 1933. The solubility of nitrogen in water at 50, 75 and 100 from 25 to 1000 atmospheres. J. Am. Chem. Soc. 55, 947–953.

Wigand, M., Kaszuba, J.P., Carey, J.W., Hollis, W.K., 2009. Geochemical effects of CO_2 sequestration on fractured wellbore cement at the cement/caprock interface. Chem. Geol. 265, 122–133.

Wolterbeek, T.K.T., Cornelissen, E.K., Hangx, S.J.T., Spiers, C.J., 2021a. Impact of downhole pressure and fluid-access on the effectiveness of wellbore cement expansion additives. Cement Concr. Res. 147, 106514.

Wolterbeek, T.K.T., Cornelissen, E.K., Nolan, S., Todea, F., Stam, W., Roggeband, S.M., Dam, L., van Riet, E.J., Ruckert, F., Keultjes, W.J.G., 2021b. Restoration of annular zonal isolation using localized casing expansion (LCE) technology: a proof of concept based on laboratory studies and field trial results. J. Petrol. Sci. Eng. 197, 108103.

Wolterbeek, T.K.T., Hangx, S.J.T., 2021. Remediation of annular gas migration along cemented wellbores using reactive mineral fluids: experimental assessment of sodium bicarbonate and sodium silicate-based solutions. Energies 14, 7507.

Wolterbeek, T.K.T., Hangx, S.J.T., 2023. The thermal properties of set Portland cements – a literature review in the context of CO_2 injection well integrity. Int. J. Greenh. Gas Control 126, 103909.

Wolterbeek, T.K.T., Hangx, S.J.T., Spiers, C.J., 2016a. Effect of CO_2-induced reactions on the mechanical behaviour of fractured wellbore cement. Geomechanics for Energy and the Environment 7, 26–46.

Wolterbeek, T.K.T., Peach, C.J., Raoof, A., Spiers, C.J., 2016b. Reactive transport of CO_2-rich fluids in simulated wellbore interfaces: flow-through experiments on the 1–6 m length scale. Int. J. Greenh. Gas Control 54, 96–116.

Wolterbeek, T.K.T., Peach, C.J., Spiers, C.J., 2013. Reaction and transport in wellbore interfaces under CO_2 storage conditions: experiments simulating debonded cement–casing interfaces. Int. J. Greenh. Gas Control 19, 519–529.

Wolterbeek, T.K.T., Raoof, A., 2018. Meter-scale reactive transport modeling of CO_2-rich fluid flow along debonded wellbore casing-cement interfaces. Environ. Sci. Technol. 52, 3786–3795.

Wolterbeek, T.K.T., Ruckert, F., van Moorsel, S.G., Cornelissen, E.K., 2019. Reactive transport and permeability evolution in wellbore defects exposed to periodic pulses of CO_2-rich water. Int. J. Greenh. Gas Control 91, 102835.

Yalcinkaya, T., Radonjic, M., Willson, C.S., Bachu, S., 2011. Experimental study on a single cement-fracture using CO_2 rich brine. Energy Procedia 4, 5335–5342.

Yan, W., Zhao, G.-Y., Chen, G.-J., Guo, T.-M., 2001. Interfacial tension of (methane + nitrogen) + water and (carbon dioxide + nitrogen) + water systems. J. Chem. Eng. Data 46, 1544–1548.

Zhang, M., Bachu, S., 2011. Review of integrity of existing wells in relation to CO_2 geological storage: what do we know? Int. J. Greenh. Gas Control 5, 826–840.